Retrievals of sulfur dioxide from the Global Ozone Monitoring Experiment 2 (GOME-2) using an optimal estimation approach: Algorithm and initial validation

C. R. Nowlan,[1] X. Liu,[1] K. Chance,[1] Z. Cai,[2] T. P. Kurosu,[1] C. Lee,[3] and R. V. Martin[1,4]

Received 15 February 2011; revised 9 May 2011; accepted 7 June 2011; published 16 September 2011.

[1] We apply an optimal estimation algorithm originally developed for retrieving ozone profiles from the Global Ozone Monitoring Experiment (GOME) and the Ozone Monitoring Instrument (OMI) to make global observations of sulfur dioxide from the Global Ozone Monitoring Experiment 2 (GOME-2) on the MetOp-A satellite. Our approach combines a full radiative transfer calculation, retrieval algorithm, and trace gas climatologies to implicitly include the effects of albedo, clouds, ozone, and SO_2 profiles in the retrieval. Under volcanic conditions, the algorithm may also be used to directly retrieve SO_2 plume altitude. Retrieved SO_2 columns over heavy anthropogenic pollution typically agree with those calculated using a two-step slant column and air mass factor approach to within 10%. Retrieval uncertainties are quantified for GOME-2 SO_2 amounts; these are dominated by uncertainty contributions from noise, surface albedo, profile shape, correlations with other retrieved parameters, atmospheric temperature, choice of wavelength fitting window, and aerosols. When plume altitudes are also simultaneously retrieved, additional significant uncertainties result from uncertainties in the a priori altitude, the model's vertical layer resolution, and instrument calibration. Retrieved plume height information content is examined using the Mount Kasatochi volcanic plume on 9 August 2008. An a priori altitude of 10 km and uncertainty of 2 km produce degrees of freedom for signal of at least 0.9 for columns >30 Dobson units. GOME-2 estimates of surface SO_2 are compared with in situ annual means over North America in 2008 from the Clear Air Status and Trends Network (CASTNET; $r = 0.85$, $N = 65$) and Air Quality System (AQS) and National Air Pollution Surveillance (NAPS; $r = 0.40$, $N = 438$) networks.

Citation: Nowlan, C. R., X. Liu, K. Chance, Z. Cai, T. P. Kurosu, C. Lee, and R. V. Martin (2011), Retrievals of sulfur dioxide from the Global Ozone Monitoring Experiment 2 (GOME-2) using an optimal estimation approach: Algorithm and initial validation, *J. Geophys. Res.*, *116*, D18301, doi:10.1029/2011JD015808.

1. Introduction

[2] Sulfur dioxide (SO_2) in the atmosphere has important impacts on chemistry and climate at both local and global levels. Anthropogenic sources account for roughly 70% of global emissions [*Faloona*, 2009]. These are primarily fossil fuel burning, with smaller contributions from smelting and biomass burning. Natural sources account for the remainder of SO_2 emissions. These include contributions from marine phytoplankton through the production and oxidation of dimethyl sulfide (~20%), volcanic activity (~7%–10%), and a small contribution from soil and vegetation decay through the production of H_2S.

[3] SO_2 oxidizes in the atmosphere to sulfate, and both are removed by wet or dry deposition. In the boundary layer and lower troposphere, SO_2 has a lifetime of 1–3 days [*Faloona*, 2009], while sulfate has a lifetime of 3–7 days. The effects of SO_2 emissions include impacts on air quality and mortality rates [*Pope and Dockery*, 2006], regional radiative forcing [*Haywood and Boucher*, 2000], and acid rain through wet deposition. Tropospheric SO_2 emissions that result in aerosol formation in the upper troposphere may also influence stratospheric humidity levels [*Notholt et al.*, 2005].

[4] When SO_2 is injected into the stratosphere during particularly explosive volcanic eruptions, the resulting sulfate aerosols can remain in the atmosphere for over a year [*Forster et al.*, 2007], affecting global climate through the scattering of solar radiation and absorption of longwave radiation. The induced radiative forcing can influence surface temperature and stratospheric circulation patterns, and modify internal

[1]Atomic and Molecular Physics Division, Harvard-Smithsonian Center for Astrophysics, Cambridge, Massachusetts, USA.
[2]Key Laboratory of Middle Atmosphere and Global Environment Observation, Institute of Atmospheric Physics, Chinese Academy of Sciences, Beijing, China.
[3]National Institute of Meteorological Research, Korea Meteorological Administration, Seoul, South Korea.
[4]Department of Physics and Atmospheric Science, Dalhousie University, Halifax, Nova Scotia, Canada.

0148-0227/11/2011JD015808

climate modes [*Forster et al.*, 2007]. Stratospheric ozone is also affected through the supply of heterogeneous reaction surfaces for ozone loss [*World Meteorological Organization*, 2007].

[5] Satellite measurements of SO_2 are useful for providing global coverage of emission sources and for observing the often remote and unpredictable locations of volcanic eruptions. The strong absorption of solar radiation by SO_2 in the ultraviolet was first used to observe SO_2 from space with the Total Ozone Mapping Spectrometer (TOMS) on the Nimbus 7 spacecraft during the El Chichón volcanic eruption in 1982 [*Krueger*, 1983]. SO_2 has since been measured from space in the ultraviolet using the Solar Backscatter Ultraviolet instrument (SBUV/2) [*McPeters*, 1993], the Global Ozone Monitoring Experiment (GOME) on ERS-2 [*Eisinger and Burrows*, 1998; *Khokhar et al.*, 2005; *Thomas et al.*, 2005], the Scanning Imaging Absorption Spectrometer for Atmospheric Chartography (SCIAMACHY) on Envisat [*Afe et al.*, 2004; *Lee et al.*, 2008], the Ozone Monitoring Instrument (OMI) on Aura [*Krotkov et al.*, 2006; *Carn et al.*, 2007; *Yang et al.*, 2007; *Carn et al.*, 2008; *Yang et al.*, 2009a], and the Global Ozone Monitoring Experiment 2 (GOME-2) on MetOp-A [*Bobrowski et al.*, 2010; *Heue et al.*, 2010]. Infrared sounders are also able to measure SO_2 from satellites, including, but not limited to, the Atmospheric Infrared Sounder (AIRS) [*Carn et al.*, 2005], Tropospheric Emission Spectrometer (TES) [*Clerbaux et al.*, 2008], and Infrared Atmospheric Sounding Interferometer (IASI) [*Clarisse et al.*, 2008; *Karagulian et al.*, 2010], but with less sensitivity to boundary layer SO_2 than those instruments measuring backscattered UV radiation.

[6] GOME-2 [*Munro et al.*, 2006] is the most recently deployed satellite instrument able to measure SO_2 in the UV. GOME-2 is a follow-on instrument to the original GOME instrument [*European Space Agency*, 1995] (on orbit since April 1995), and flies on the European Organisation for the Exploitation of Meteorological Satellites (EUMETSAT) MetOp-A satellite, which was launched on 19 October 2006. GOME-2 measures backscattered radiation from 240–790 nm in four channels with spectral resolutions of 0.23–0.53 nm (Z. Cai et al., Validation of Global Ozone Monitoring Experiment 2 reflectance in ultraviolet, manuscript in preparation, 2011), and a nominal spatial resolution of 80×40 km^2.

[7] SO_2 is traditionally retrieved from UV spectra by fitting a slant column density (SCD) of SO_2 in the observing path using the ratio of observed backscattered solar radiation to an observed solar irradiance spectrum. The slant column is converted to a vertical column density (VCD) using an air mass factor (AMF), which represents the ratio of the SCD to the VCD. The AMF is dependent on the vertical profile of SO_2, the fractional coverage of clouds and their altitude in the instrument's field of view, molecular and aerosol scattering, surface albedo, and the ozone profile and column, which limit the penetration depth of photons in the UV. In the spectral range from 310 to 330 nm (the approximate region of traditional SO_2 retrievals), the AMF is highly dependent on wavelength because of the large gradient in ozone absorption as a function of wavelength (varying, for example, by 10%–30% between 313 and 320 nm, depending on viewing geometry and ozone amount). The AMF is determined in a variety of ways, including globally uniform AMFs based on typical radiative transfer parameters [e.g., *Khokhar et al.*, 2005], look-up tables (e.g., the Tropospheric Emission Monitoring Internet Service, http://www.temis.nl/), or a full radiative transfer calculation for each local ground pixel [e.g., *Lee et al.*, 2009]. In addition, the absorption of ozone is somewhat spectrally correlated to that of SO_2, so that an accurate retrieval of SO_2 depends on properly accounting for ozone. *Lee et al.* [2008] showed that improved physical representation of several radiative transfer parameters, including the treatment of wavelength dependencies in the AMF, could lower biases in SO_2 slant column fitting results.

[8] In this paper, we apply an optimal estimation algorithm originally developed at the Smithsonian Astrophysical Observatory (SAO) for retrieving ozone profiles and tropospheric ozone from the GOME and OMI instruments [*Liu et al.*, 2005, 2010] to retrieve SO_2. This algorithm applies a full radiative transfer calculation in combination with trace gas climatological profiles to implicitly include the effects of clouds, surface albedo, ozone absorption and scattering in the retrieval, thereby removing the need for a separate air mass factor calculation. The full physical treatment of radiative transfer processes also allows a direct retrieval of SO_2 plume altitude in specific cases, and allows a simultaneous retrieval of the ozone profile to assist in accurate SO_2 retrievals. Furthermore, problems in dealing with strong SO_2 absorption because of assumptions made about the optical path and its wavelength independence inherent in many other SO_2 retrieval algorithms [see, e.g., *Eisinger and Burrows*, 1998; *Khokhar et al.*, 2005; *Yang et al.*, 2007; *Bobrowski et al.*, 2010] (also see discussion by *Yang et al.* [2010]) are not an issue in our algorithm, which uses a full radiative transfer calculation to directly retrieve SO_2.

[9] In this study, we apply the algorithm to retrieve SO_2 columns from the GOME-2 instrument. The study has two main objectives: first, to assess the performance of the ozone profiling optimal estimation algorithm for retrieving SO_2 using GOME-2 data and, second, to assess the data quality of SO_2 measurements from GOME-2. The optimal estimation approach is used throughout the paper, with the exceptions of sections 3.2 and 4.2, which describe the traditional slant column fitting approach and comparisons of the optimal estimation approach with that algorithm.

[10] The paper is structured as follows: Section 2 introduces GOME-2 and the atmospheric chemistry model and validation data. Section 3 presents the algorithm in detail and discusses improvements in GOME-2 calibration. Section 4 presents retrieval cases and algorithm comparisons, while section 5 discusses uncertainties and characterization of these retrievals. Section 6 presents comparisons to surface in situ measurements of SO_2 over the United States and Canada.

2. Data and Model Description

2.1. GOME-2

[11] GOME-2 has four spectral channels, each with a holographic grating and 1024 pixel photodiode array detector to measure dispersed light in the wavelength regions: (1) 240–314 nm, (2) 310–403 nm, (3) 397–604 nm, and (4) 593–790 nm (wavelength limits are defined where 10% of signal occurs in that channel) [*EUMETSAT*, 2006]. In the region of strong SO_2 absorption (300–330 nm), the

spectral resolution is approximately 0.23–0.25 nm in channel 1 and 0.30–0.32 nm in channel 2, and the sampling frequency is ~0.12 nm per detector pixel.

[12] MetOp-A is in a Sun-synchronous orbit at an altitude of 817 km with a local equatorial crossing time of 9:30 AM in the descending node. The nominal GOME-2 swath is 1920 km wide, with 24 spectra collected in the forward scan (east to west), and 8 in the flyback scan. Each forward scan measurement has a footprint of 80 km (cross track) × 40 km (along track), while back-scan pixels are 240 × 40 km^2. In addition to backscattered radiance measurements, GOME-2 measures several solar irradiance reference spectra with a diffuser once per day. Radiometric throughput degradation has been observed in these spectra; as of May 2010, solar irradiance throughput in channel 2 was ~45–50% of that in January 2007.

[13] Channels 1 and 2 are each further divided into bands A and B to account for the large dynamic range of backscattered light intensities at these wavelengths. The integration time of band 1A is eight times that of the other channels, and any use of retrievals combining band 1A with other bands requires the coadding of other bands, resulting in an effective nominal band 1A spatial resolution of 640 × 40 km^2 in the forward scan. The division between bands 1A and 1B was at 307 nm until 10 December 2008 08:00:00 UTC, when it was changed to 283 nm. (The division between bands 2A and 2B occurs at 299 nm, well below the 10% intensity channel limit of 310 nm, thus band 2A signal is too weak to be useful for our retrievals.)

[14] In this study we use GOME-2 radiometrically calibrated level 1B spectra determined using the Product Processing Facility (PPF) version 4.0.0.

2.2. GEOS-Chem Atmospheric Chemistry Model

[15] The GEOS-Chem 3-D global tropospheric chemistry model [*Bey et al.*, 2001] is used in this study to define SO_2 profile shapes, for air mass factor calculations, and for calculations of surface SO_2. In this study we use GEOS-Chem version v8-01-04 (http://www.geos-chem.org/), which is driven by GEOS-4 (Goddard Earth Observing System) meteorological analyses on 30 pressure levels on a grid of 2° latitude by 2.5° longitude. The SO_2 inventory is updated to 2006, as described by *Lee et al.* [2009], and includes anthropogenic and natural sources, with volcanic activity for 2006. The SO_2 average is determined from the model for local times between 09:00 and 11:00 to coincide with GOME-2 overpasses.

2.3. Surface Observations

2.3.1. Clear Air Status and Trends Network

[16] The Clear Air Status and Trends Network (CASTNET) is a network administered by the Environmental Protection Agency (EPA) consisting of mostly rural and semirural stations measuring ambient background concentrations of a variety of pollutants. SO_2 concentrations are measured as a weekly average by dry deposition with three-stage filter packs [*Clarke et al.*, 1997]. We use CASTNET SO_2 measurements where a GOME-2 overpass falls within the weekly integration time.

2.3.2. Air Quality System

[17] The EPA Air Quality System (AQS) is a series of sites monitoring ambient air quality across the United States, with site locations varying from regional background to urban and industrial locations. AQS SO_2 is measured using continuous gas monitors, and is generally reported hourly. We use SO_2 values within an hour of GOME-2 overpasses.

2.3.3. National Air Pollution Surveillance Network

[18] The National Air Pollution Surveillance (NAPS) network is a series of measurement sites monitoring air quality across Canada and administered by Environment Canada. Sites are generally located in populated areas, and typically make hourly measurements of SO_2. We use NAPS SO_2 measured within an hour of GOME-2 overpasses.

3. Retrieval Algorithm

3.1. Optimal Estimation

3.1.1. SO_2 Vertical Column Density Retrieval

[19] The SO_2 retrieval algorithm used in this study is based on the OMI ozone profile retrieval algorithm described by *Liu et al.* [2010], which itself is based on the ozone profile algorithm originally developed for GOME-1 [*Liu et al.*, 2005]. The algorithm uses an optimal estimation (OE) approach [*Rodgers*, 2000], which attempts to minimize the difference between an observation vector $\mathbf{y}$ and a forward model $\mathbf{F}(\mathbf{x})$, within measurement errors represented by noise covariance matrix $\mathbf{S}_\epsilon$, while simultaneously minimizing the difference between a state vector $\mathbf{x}$ of retrieved parameters and an a priori vector $\mathbf{x}_a$ with an associated a priori uncertainty covariance matrix $\mathbf{S}_a$.

[20] The nonlinear problem can be solved iteratively by minimizing a representative cost function and linearizing about a current guess $\mathbf{x}_i$, with the next state at iteration $i+1$ represented by

$$\mathbf{x}_{i+1} = \mathbf{x}_i + \left(\mathbf{K}_i^T \mathbf{S}_\epsilon{}^{-1} \mathbf{K}_i + \mathbf{S}_a{}^{-1}\right)^{-1} \cdot \left[\mathbf{K}_i^T \mathbf{S}_\epsilon{}^{-1}(\mathbf{y} - \mathbf{F}(\mathbf{x}_i)) - \mathbf{S}_a{}^{-1}(\mathbf{x}_i - \mathbf{x}_a)\right], \quad (1)$$

where $\mathbf{K}$ is a weighting function matrix with elements $K = \partial F(\mathbf{x})/\partial x$.

[21] In our implementation, the measurement $\mathbf{y}$ contains the logarithm of the ratio of the backscattered radiance spectrum to the solar mean reference spectrum (effective optical depth). We typically use the spectral range 312–330 nm in band 2B. The state vector $\mathbf{x}$ contains the following 37 retrieved elements (summarized in Table 1) for the band 2B retrieval: the total SO_2 vertical column; vertical columns of NO_2, BrO, and HCHO; ozone on 24 vertical levels; the effective surface albedo in the retrieved spectral range; the effective cloud fraction; a scaling of the Ring spectrum [*Sioris and Evans*, 2000]; a relative wavelength shift between the radiance and irradiance spectra; a wavelength correction for the ozone absorption cross section; and a third-order polynomial to reduce remaining radiance/irradiance low-order residuals. Retrievals using an additional band in channel 1 also retrieve additional independent values for the band's surface albedo, undersampling correction, Ring correction, and wavelength shifts.

[22] The atmosphere is modeled with the Vector Linearized Discrete Ordinate Radiative Transfer model (VLIDORT) [*Spurr*, 2006], which is used to both simulate radiances and calculate analytic weighting functions. We perform radiative transfer calculations at a selected wavelength spacing ($\Delta\lambda$ =

Table 1. Parameters Retrieved in the Optimal Estimation Algorithm[a]

Retrieved Parameter	A Priori and a Priori Error	Cross Section	Band Independent
SO_2 vertical column	GEOS-Chem [*Lee et al.*, 2009], ϵ_{ap} = 10,000 DU	*Bogumil et al.* [2003] (203, 223, 243, 273, 293 K)	no
SO_2 plume altitude	10 km (varies with case), ϵ_{ap} = 2 km (varies with case)		no
NO_2 vertical column	GEOS-Chem (troposphere), *McLinden et al.* [2000] (stratosphere), ϵ_{ap} = 50%	*Vandaele et al.* [1998] (220 K)	no
BrO vertical column	*McLinden et al.* [2000], ϵ_{ap} = 100%	*Wilmouth et al.* [1999] (228 K)	no
HCHO vertical column	GEOS-Chem, ϵ_{ap} = 50%	*Meller and Moortgat* [2000] (298 K)	no
O_3 (24 vertical layers)	Profile climatology [*McPeters et al.*, 2007], ϵ_{ap} = climatology	*Liu et al.* [2007] from *Brion et al.* [1993] (218, 228, 243, 295 K)	no
Effective surface albedo	OMI climatology [*Kleipool et al.*, 2008], ϵ_{ap} = 0.05		yes
Effective cloud fraction	Calculated from 347 nm radiance, ϵ_{ap} = 0.05		no
Ring effect scaling	1.9, ϵ_{ap} = 1.0	*Sioris and Evans* [2000]	yes
λ shift	0.0 nm, ϵ_{ap} = 0.01 nm		yes
O_3 cross section λ shift	0.0 nm, ϵ_{ap} = 0.01 nm		yes
Radiance/irradiance polynomial	$a_0 + a_1(\lambda - \overline{\lambda}) + a_2(\lambda - \overline{\lambda})^2 + a_3(\lambda - \overline{\lambda})^3$, a_0 = 0, a_1 = 0, a_2 = 0, a_3 = 0, ϵ_{ap} = 0.3, 0.1, 0.1, 0.1		yes
Undersampling	0, ϵ_{ap} = 0.7	*Chance et al.* [2005]	channel 1 only

[a]For channel 2 (band 2B) retrievals, these consist of 37 fitted parameters, including ozone in 24 vertical layers. An additional SO_2 plume altitude term can be retrieved under certain conditions (see text). For retrievals that also include channel 1 (band 1B), additional terms are included for the band's surface albedo, Ring effect scaling, wavelength shifts, and undersampling.

1 nm for $\lambda \leq 295$ nm; $\Delta\lambda = 0.5$ nm for 295 nm $< \lambda \leq 308$ nm; $\Delta\lambda = 0.2$ nm for $\lambda > 308$ nm) and interpolate to every 0.05 nm using weighting functions. The radiance on the fine wavelength grid is then convolved to lower resolution with the instrument line shape. With this interpolation scheme, radiance calculated at the GOME-2 resolution is typically accurate to better than 0.1% as compared to that calculated every 0.05 nm. The forward model is run with full polarization calculations performed at six wavelengths (10 when channel 1 is added), as well as in scalar mode at all wavelengths. The corrections to scalar calculations due to the neglect of polarization are derived from these six wavelengths and are interpolated to the other wavelengths. This results in faster forward model calculations than if polarization were included at all calculated wavelengths. For isolated volcanic cases with very large SO_2 amounts where small but higher-resolution features in the SO_2 absorption spectrum become more important in the fit, fitting residuals are minimized by performing calculations on a wavelength grid as fine as $\Delta\lambda$ = 0.02 nm.

[23] The atmosphere is modeled on 50 pressure layers, spaced at approximately 1.3 km, with one layer at the cloud altitude. Temperature profiles are from daily National Centers for Environmental Prediction (NCEP) reanalyses [*Kalnay et al.*, 1996]. Surface pressures are determined from the ground pixel terrain height provided in the GOME-2 L1B data.

[24] The first-guess and a priori surface albedo is determined at 347 nm from the OMI surface reflectance climatology [*Kleipool et al.*, 2008], and the effective albedo is allowed to vary during the retrieval with an a priori uncertainty of 0.05. This initial albedo is used in combination with the measured radiance to irradiance ratio at 347 nm to determine an initial effective cloud fraction in the UV. The effective cloud fraction is allowed to vary in the retrieval with an a priori uncertainty of 0.05. The surface albedo and effective cloud fraction are highly correlated, but are self-consistent with each other and the total reflectivity. During a typical retrieval they each tend to vary less than 0.02 from their a priori values. The cloud altitude is fixed using the retrieved cloud altitude pressure from the Fast Retrieval Scheme for Clouds from the Oxygen A band (FRESCO) cloud algorithm [*Koelemeijer et al.*, 2001], determined from reflectance in the O_2 *A* band in channel 4 and provided in the level 1B data files. Aerosols are not modeled directly in the retrieval; rather, their effects are partially taken up by the effective surface albedo [*Liu et al.*, 2010] and effective cloud fraction, with corresponding uncertainties from excluding aerosols examined in section 5. The retrieval is highly sensitive to albedo, cloud fraction, and cloud altitude pressure, and currently does not provide accurate results over ice and snow where the FRESCO algorithm has difficulty in distinguishing between reflecting surfaces. As a result, in this paper we exclude ground pixels flagged by FRESCO as being over ice or snow. Trace gas distributions, clouds, and other atmospheric and surface properties are assumed to be homogeneous over the ground footprint.

[25] The high-resolution solar reference spectrum is from *Chance and Kurucz* [2010]. The first-order Ring effect from rotational Raman scattering is calculated directly in the forward model [*Sioris and Evans*, 2000], while its scaling parameter is retrieved in the spectral fitting.

[26] Undersampling of the reference spectrum occurs when less than ~3 pixels are sampled over the full width at half maximum (FWHM) of the instrument line shape [*Chance et al.*, 2005]. An undersampling correction is applied in channel 1 only, where the resolution approaches twice the sampling frequency.

[27] Monthly SO_2 profiles are from GEOS-Chem updated to 2006 emissions [*Lee et al.*, 2009], as previously discussed in section 2.2, and interpolated using cubic interpolation to the ground pixel center location. The SO_2 profile shape is kept constant while the total SO_2 column is allowed to vary in the retrieval. SO_2 temperature-dependent cross sections are from *Bogumil et al.* [2003]. The a priori total column of SO_2 can be highly uncertain, particularly in the case of volcanic eruptions, and because the day-to-day distribution from transport is likely not well represented in a monthly

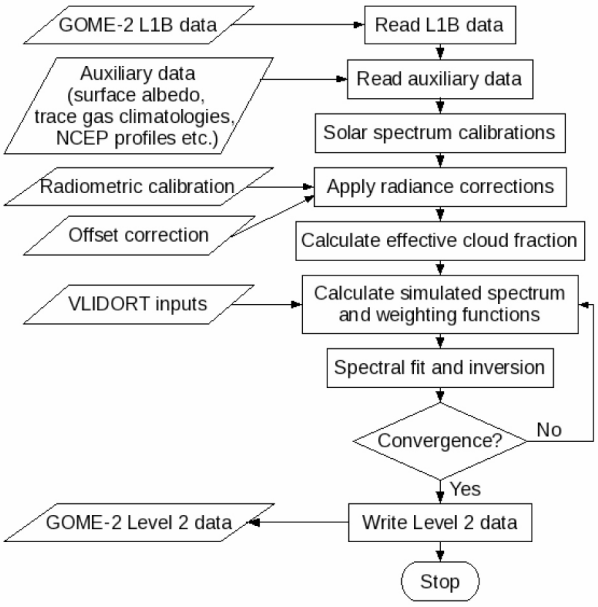

Figure 1. Flow diagram of GOME-2 optimal estimation algorithm.

climatology. The uncertainty in the modeled SO_2 on an individual observation basis can therefore be very large. For consistency, and to avoid loss of information, we effectively leave SO_2 unconstrained in the retrieval by assigning very large a priori errors of 10000 Dobson units (DU, 1 DU = 2.69×10^{16} molecules cm^{-2}). (Typical large anthropogenic emissions viewed from GOME-2 are 1–5 DU, while the largest volcanic column observed to date from space was on the order of 1000 DU, as viewed by the OMI instrument [*Yang et al.*, 2009a] during the October 2005 eruption of Sierra Negra, Galapagos Islands, Ecuador.) Although for consistency we may refer to the SO_2 total column derived from GEOS-Chem as the "a priori," the large uncertainty on the a priori SO_2 VCD means that the retrieved solution is essentially independent from the SO_2 a priori column amount (although it is still dependent on the profile shape).

[28] Ozone profiles are retrieved at 24 layers. A priori ozone profiles are from the ozone profile climatology by *McPeters et al.* [2007], and first-guess ozone profiles are typically from a previous retrieval. The climatology's standard deviations are used for a priori uncertainties. Ozone absorption is calculated using temperature-dependent cross sections derived from the work of *Brion et al.* [1993] by *Liu et al.* [2007].

[29] NO_2, BrO, and HCHO total vertical column densities are also retrieved, with a priori uncertainties of 50% for NO_2 and HCHO, and 100% for BrO. NO_2 and HCHO tropospheric profiles are monthly GEOS-Chem climatologies. Stratospheric NO_2 and BrO profiles are from chemical transport model simulations [*McLinden et al.*, 2000]. Cross sections are from *Vandaele et al.* [1998] (NO_2 at 220 K), *Wilmouth et al.* [1999] (BrO at 228 K), and *Meller and Moortgat* [2000] (HCHO at 298 K). Tests leaving NO_2 unconstrained produce NO_2 columns that agree fairly well spatially with NO_2-optimized retrievals in channel 3, although the NO_2 is typically very noisy and overestimated by a factor of ~2–3. The 50% uncertainty ensures values are somewhat constrained to climatologies; eventual implementation of separately retrieved trace gas columns as a priori could help to eliminate small potential biases in retrieved SO_2.

[30] Additional corrections are also fit to represent wavelength shifts in (1) the relative wavelength detector pixel registration between the radiance and solar mean reference spectrum and (2) the ozone cross section relative to each radiance spectrum. A third-order multiplicative polynomial applied to the solar irradiance is retrieved to account for additional low-order differences between the irradiance and radiance that remain after the calibration described in section 3.4.2, similar to the degradation correction applied by *Liu et al.* [2005] to GOME-1 data. The use of the polynomial tends to reduce these low-order residuals so that mean fitting residuals are typically reduced by 20%–30%. Very similar SO_2 amounts can also be retrieved by fitting a third-order surface albedo; however, the resultant albedo is not always sensible, indicating remaining low-order effects that cannot be accounted for in an entirely physical retrieval.

[31] A schematic of the optimal estimation algorithm is shown in Figure 1. One GOME-2 orbit of ~16,000 ground pixels takes approximately 6 h to process on an Intel Xeon X5365 3GHz processor, roughly two orders of magnitude longer than for the SCD/AMF product. We are able to process one month of ~440 orbits in parallel on the Smithsonian Institution cluster.

3.1.2. SO_2 Plume Altitude Retrieval

[32] SO_2 retrievals are treated differently under explosive volcanic conditions where the SO_2 plume altitude is likely at a higher altitude than expected from the GEOS-Chem model. Recent work [*Yang et al.*, 2009b, 2010] has demonstrated SO_2 plume altitude retrievals are possible by taking advantage of the changing penetration depth of photons across the UV. This characteristic can be readily exploited by an algorithm such as ours which implements a full vertically resolved radiative transfer code. For these cases, we replace the GEOS-Chem profile retrieval with a Gaussian plume having a FWHM of 0.5 km. The SO_2 plume altitude is retrieved directly by the addition of a term in the retrieval vector $\mathbf{x}$ to represent the altitude of the plume's peak. The first-guess plume altitude is currently chosen on an observation-by-observation basis, using observations from other sensors including satellite-based aerosol lidar and ground-based radar.

3.2. Slant Column Density Two-Step Approach

[33] We also perform SO_2 retrievals using a slant column density and air mass factor approach for comparison with the optimal estimation algorithm. This approach is an SO_2-optimized version of previous algorithms developed for slant column fitting [*Chance et al.*, 2000; *Martin et al.*, 2002] and uses AMF calculations described by *Lee et al.* [2009].

3.2.1. Slant Column Density Retrieval

[34] In this study, we derive slant column densities of SO_2 using direct fitting of radiance spectra in the wavelength region of 312–330 nm. The direct fit applies laboratory cross sections directly in the calculation, rather than fitting the high-resolution absorption spectral components as is sometimes done in UV-visible remote sounding. SO_2 is fit

Table 2. Summary of Measurements and Error Contributions for Six Individual Observations Chosen for Characterization and Error Analysis[a]

Description	Clean Marine	Polluted		Volcanic		
		Clear	Partly Cloudy	Effusive	Moderate[b]	Heavy[b]
Observation Conditions						
Orbit	9350	7947	7947	9350	9379	9379
Viewing zenith angle	−35.9°	−15.2°	−50.8°	3.1°	44.0°	15.2°
Solar zenith angle	41.3°	36.4°	39.8°	33.9°	35.6°	37.7°
Cloud fraction	0.48	0.03	0.42	0.07	0.70	0.36
Cloud top pressure	777.4 hPa	706.1 hPa	641.7 hPa	714.6 hPa	855.1 hPa	664.0 hPa
Surface albedo	0.08	0.10	0.05	0.08	0.06	0.06
Latitude	10.0°	37.6°	26.7°	18.6°	47.0°	45.6°
Longitude	−164.8°	116.7°	107.3°	−157.6°	−155.0°	−162.2°
A priori SO_2 VCD	0.01 DU	1.4 DU	0.4 DU	0.1 DU	0.1 DU	0.1 DU
Retrieved SO_2 VCD	0.01 DU	4.0 DU	6.0 DU	12.0 DU	22.7 DU	280.2 DU
A priori SO_2 plume altitude	N/A	N/A	N/A	N/A	10.0 km	10.0 km
Retrieved SO_2 plume altitude	N/A	N/A	N/A	N/A	6.4 km	9.6 km
Model Parameter Errors (Systematic)[c]						
Cloud top pressure (53 hPa)	0.00 DU	0.6	25.0	1.2	0.1/1.2	0.2/0.3
Initial surface albedo (0.02)	0.00 DU	10.1	9.4	8.8	7.1/22.5	0.1/0.1
Profile shape (variability and 10% bias)	0.01 DU	12.8	15.3	23.4	N/A	N/A
Volcanic plume FWHM (0.5 km versus 2 km)	N/A	N/A	N/A	N/A	7.2/23.3	3.2/4.5
Aerosols (GEOS-Chem off versus on)	0.00 DU	11.1	4.6	2.4	see text	see text
SO_2 cross section (4%)	0.00 DU	3.9	3.9	3.9	3.9/0.0	3.9/0.0
SO_2 cross section λ (0.01 nm)	0.01 DU	1.4	1.2	0.2	4.6/14.6	0.5/0.5
O_3 cross section (1%)	0.00 DU	0.3	0.5	0.2	0.8/2.4	0.3/3.4
NO_2 cross section (5%)	0.00 DU	0.4	1.7	0.1	0.1/0.4	0.0/0.0
BrO cross section (8%)	0.00 DU	0.1	0.0	0.0	0.0/0.3	0.0/0.0
HCHO cross section (10%)	0.00 DU	0.6	0.0	0.0	0.0/0.5	0.0/0.0
Temperature profile (3 K, all layers)	0.08 DU	11.2	13.0	2.8	6.6/25.1	1.0/0.7
Offset correction (0.05 DU)	0.07 DU	2.3	3.6	0.8	0.1/0.1	0.0/0.0
Radiance correction (10%)	0.05 DU	0.8	1.5	10.3	3.4/28.5	2.8/6.1
Slit shape (preflight versus retrieved)	0.20 DU	5.0	13.2	4.3	0.7/0.5	0.5/0.4
Retrieval λ window and polynomials	0.02 DU	11.0	18.9	10.0	8.6/27.8	3.0/6.0
Model Parameter Errors (Random)[c]						
SO_2 cross section (0.2%)	0.00 DU	0.3	0.2	0.2	0.1/0.7	0.0/0.1
SO_2 cross section λ (0.002 nm)	0.00 DU	0.2	0.2	0.1	0.0/0.3	0.0/0.1
O_3 cross section (0.2%)	0.11 DU	6.2	2.2	0.9	0.8/1.6	0.0/0.0
O_3 cross section λ (0.002 nm)	0.01 DU	2.3	0.2	0.3	0.1/0.8	0.0/0.0
Wavelength calibration (0.002 nm)	0.04 DU	3.7	6.6	1.5	0.3/1.2	0.1/0.1
Forward Model Errors[c]						
0.05 nm versus 0.01 nm grid	0.04 DU	4.9	1.8	3.4	1.4/4.8	0.5/1.8
1.3 km (default) versus 0.5 km vertical layers	0.00 DU	4.2	8.4	8.5	8.0/42.0	0.8/2.5
Polarization interpolation	0.01 DU	3.6	0.4	1.6	0.1/1.4	0.9/1.7
Smoothing and Measurement Noise Error						
Smoothing error	0.00 DU	29.1	28.2	26.9	6.0/29.6	1.8/0.9
Measurement noise error	0.21 DU	24.9	31.2	8.9	8.5/6.3	2.9/1.1

[a]The uncertainties in the error sources used for the error analysis are shown in brackets.
[b]Errors are vertical column density/altitude.
[c]All units are in percent (%), unless otherwise specified.

using a cross section from *Bogumil et al.* [2003] at 293 K. Cross sections from *Vandaele et al.* [2009] (298 K) improve SO_2 estimated fitting uncertainties by 10%, but, as these cross sections are not available at multiple temperatures in our atmospheric temperature range, we use the work of *Bogumil et al.* [2003] for consistency with the OE algorithm where the vertical profile of SO_2 is fully represented in the forward model, and the temperature-dependent cross sections must be included. O_3 is included in the fit using cross sections from *Brion et al.* [1993] at 218 and 273 K, as well as NO_2, BrO, and HCHO, using the cross sections described in section 3.1.1. A Ring effect vector is fit using the formulation of *Chance and Spurr* [1997]. A wavelength shift representing the relative radiance to irradiance wavelength registration is also fit. The wavelength-dependent radiative effects of aerosols, surface albedo, and uncertainties in instrument calibration are considered by fitting third-order polynomials for both baseline offset and multiplicative scaling.

[35] Retrieval uncertainty from noise in individual SCD retrievals varies with time because of GOME-2 throughput degradation. Its value is approximately 0.42 DU for observations of unpolluted scenes in May 2008 where the solar zenith angle is less than 70°. Retrieval uncertainty increases at high latitudes (large solar zenith angles) because of the reduction in signal. Uncertainties due to uncertainties in SO_2 cross sections are similar to those from the OE approach listed in Table 2, while we estimate systematic uncertainties of 5%–10% from ignoring the temperature dependency of

SO_2 absorption, 10% from the choice of wavelength fitting window and baseline and scaling polynomial order, and 20% from uncertainties in other parameters such as the Ring effect correction and ozone cross sections.

3.2.2. Air Mass Factor Calculation

[36] Air mass factors representing the ratio of the SCD to the VCD are calculated at 319.7 nm using the United States summer standard ozone profile, GEOS-Chem SO_2 profiles, GEOS-Chem aerosols, and the scalar LIDORT radiative transfer model, following the formulation described by *Palmer et al.* [2001], *Martin et al.* [2002], and *Lee et al.* [2009]. Uncertainties in the AMF range from approximately 12% (cloud-free) to 53% (cloudy) for observations with low SO_2 abundances and from 21% (cloud-free) to 245% (cloudy) for polluted observations [*Lee et al.*, 2009].

3.3. Offset Correction

[37] SO_2 retrievals generally have an offset that is dependent on latitude, season, viewing geometry and ozone slant column density, even where no SO_2 is expected. Possible causes include insufficient consideration of the temperature dependence of the ozone cross sections, ozone-SO_2 spectral correlations, an inaccurate model of the Ring effect in a simple spectral fit [*Lee et al.*, 2008], and stray light within the instrument [*Richter*, 2009]. Several approaches are used to correct for this offset, including methods that apply a correction to the SO_2 slant columns for the offset [*Khokhar et al.*, 2005; *Lee et al.*, 2009; *Valks et al.*, 2009], and methods that adjust the radiance spectra by a fitting residual as a form of calibration [*Krotkov et al.*, 2006; *Yang et al.*, 2007].

[38] Where vertical columns are discussed in this paper from the slant column density approach, we apply an offset correction by subtracting an offset dependent on the core-trieved O_3 slant column and a further latitude-dependent offset correction using the retrieved slant column of SO_2 over the clean Pacific, excluding SO_2 contaminated pixels (greater than 2σ of fitting uncertainty). The equatorial offset correction is generally on the order of +2 DU for SCD retrievals because of correlations with ozone and our use of a single Ring spectrum vector. The offset is negative at high latitudes.

[39] A background offset is also present in retrievals using the optimal estimation approach, with a magnitude varying from about −0.5 to 0.5 DU, depending on latitude and season. It is smaller than the offset from the SCD retrievals and less correlated to the total ozone column, likely because of the more accurate treatment of the Ring effect and ozone absorption [*Lee et al.*, 2008]. This offset can have a large impact on retrievals over locations where the SO_2 profile is heavily weighted to the surface, particularly in the presence of even small amounts of clouds, where SO_2 VCD weighting functions are small and any positive value is magnified by the algorithm. (The result is equivalent to a VCD calculated by SCD/AMF, where the SCD offset has not been removed properly, and a small AMF in a polluted region causes the VCD to be artificially large.) In order to account for this offset, the latitudinally dependent offset is calculated over the clean Pacific for one day each month, and a correction is applied to the radiance before the retrieval.

[40] Tests on 2009 data show that extending the retrieval to include the channel 1 wavelength region 290–312 nm lowers this offset to less than 0.05 DU; however, prior to the band 1A/1B division shift on 10 December 2008, the use of these wavelengths would result in a reduction of nominal spatial resolution to 640×40 km^2, as well as require the use of bands 1A and 1B, which adds two additional cocalibration requirements. In the following sections we retrieve SO_2 using band 2B only, and discuss the possibilities for retrievals using multiple bands in section 4.3.

3.4. Instrument Calibration Improvements

[41] Data retrievals are performed on spectra which have been calibrated to absolute radiance units (i.e., level 1B data). However, we find several improvements to instrument wavelength, line shape, and radiometric calibrations as well as the inclusion of accurate measurement noise estimates are required to optimize the reliability of retrievals using our algorithms. Calibrations are applied to both the optimal estimation and slant column retrievals.

3.4.1. Line Shape and Wavelength Calibration

[42] Both the wavelength to detector pixel assignments and instrument line shape must be properly represented for accurate retrievals of SO_2. As was the case with the original GOME instrument [*Liu et al.*, 2005], the slit width for GOME-2 varies as a function of position on the detector in the regions of the SO_2 and O_3 retrievals.

[43] An asymmetric Gaussian slit width and wavelength to detector pixel calibration are simultaneously determined using a least squares fit of the measured GOME-2 irradiance to a high-resolution (0.04 nm) solar reference spectrum with wavelength calibration accurate to at least 0.003 nm below 305 nm and 3×10^{-4} nm above 305 nm [*Chance and Kurucz*, 2010]. The width, shift and an asymmetry factor (Cai et al., manuscript in preparation, 2011) are determined at each detector pixel by fitting the measured solar irradiance in a 21 pixel window to the high-resolution solar reference. The retrieved FWHMs and wavelength shifts are similar to those determined during preflight instrument testing [*Siddans et al.*, 2006], but allow the derivation of a slit function below 313 nm in channel 2 (the limit of preflight-derived slit functions), the verification of the slit shape and width on orbit, and the capacity to monitor long-term changes in instrument stability (Cai et al., manuscript in preparation, 2011). Unlike for GOME [*Liu et al.*, 2005], we do not perform a wavelength-dependent wavelength adjustment on individual radiance spectra; for GOME-2 this approach produces highly variable results depending on the pixel window used in the fit. Instead, the irradiance wavelength assignments are also applied to the radiance spectra, and each radiance spectrum is adjusted by a single constant wavelength shift relative to the irradiance during the spectral fit as described in section 3.1.1.

3.4.2. Radiance Calibration

[44] Spectral fitting residuals using GOME-2 PPF 4.0.0 spectra show systematic low-order biases in the UV (Cai et al., manuscript in preparation, 2011), most likely because of uncorrected stray light, instrument throughput degradation, and insufficient polarization corrections. In band 2B, observed radiances near 315 nm are consistently smaller than simulated radiances by ~1%, while near 310 nm, they are larger by ~10%. The radiance biases are too structured to be solely accounted for by a simple low-order polynomial such as that discussed in section 3.1.1. We apply a radiance calibration correction (Cai et al., manuscript in preparation,

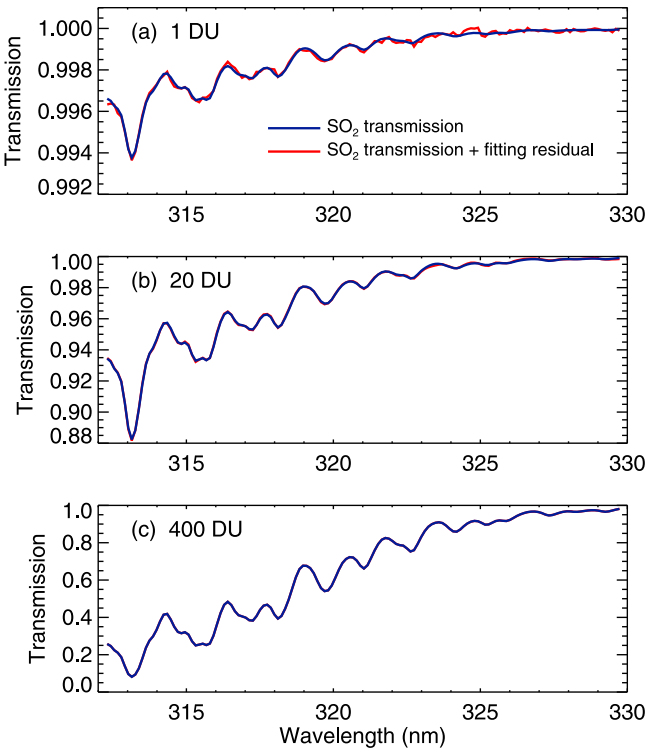

Figure 2. Transmission for an SO_2-only atmosphere with (a) 1 DU, (b) 20 DU, and (c) 400 DU of estimated SO_2 in the slant viewing path and fitting residuals from the Mount Kasatochi volcanic eruption (9 August 2008, orbit 9379).

2011) determined using simulations performed with zonal mean ozone from the Microwave Limb Sounder (MLS), similar to OMI soft calibration for ozone profile retrievals [*Liu et al.*, 2010]. Corrections are cross track dependent. They are determined using observations at latitudes of 0°–25°S from one day of data in each month to account for small temporal changes in calibration (up to 3% in band 1A and 0.8% in band 2B over 2008).

3.4.3. Measurement Error

[45] The optimal estimation approach requires accurate formulation of the measurement noise covariance $\mathbf{S}_\epsilon$. GOME-2 level 1B PPF 4.0.0 data include EUMETSAT's estimate of each radiance spectrum's total absolute uncertainty calculated from both measurement noise and systematic error sources [*EUMETSAT*, 2006], but do not provide an estimate of the measurement noise alone, whose value must be known for constructing $\mathbf{S}_\epsilon$.

[46] In order to determine the radiance uncertainty from random instrumental measurement noise only, we apply an approach that uses the Müller Matrix Element from the Calibration Key Data (collected prior to launch during instrument characterization), which describes the radiance response of the instrument as a function of scanner angle. This is used to convert the radiance back to detector counts S (A/D counts, or binary units), so that the uncertainty in the calibrated radiance R can be determined using

$$\epsilon_R = \frac{R}{S}\sqrt{\sigma^2 + \frac{S}{e}}, \tag{2}$$

where σ is the readout noise (~1.7 binary units). The term S/e represents the square of the uncertainty in binary units derived from the photon shot noise $\sqrt{Se}$, with e = 960 photoelectrons per binary unit [*EUMETSAT*, 2006]. The use of the Müller Matrix radiance response element is convenient as it allows the calculation of an accurate signal-to-noise ratio (SNR) without the use of the original binary units contained in the L1A (preradiometric calibration) data file. This approach excludes the small random error contributions from polarization and dark current corrections. The magnitudes of uncertainty estimates are confirmed by the standard deviation of spectral fitting residuals from slant column density fits, which generally agree with the Müller matrix–calculated measurement noise estimates to within 10%. Our measurement noise estimates are typically one to two orders of magnitude smaller than the combined random and systematic radiance uncertainties in the GOME-2 level 1B data files, depending on wavelength and radiance intensity.

[47] We assume noise among detector pixels on the photodiode array is uncorrelated, so that $\mathbf{S}_\epsilon$ is constructed as a diagonal matrix.

4. Retrieval Results

4.1. Spectral Fitting

[48] Figure 2 shows fitting residuals and their strength relative to transmission through an SO_2-only atmosphere for typical measurements of the SO_2 plume detected on 9 August 2008 from the Mount Kasatochi volcano in Alaska, which began an explosive eruption on 7 August 2008. Fitting residuals are approximately 0.15 to 0.2% of the logarithm of the Sun-normalized radiance for unpolluted and moderately polluted scenes. For a heavily polluted volcanic observation, such as that modeled in Figure 2c, fitting residuals are primarily systematic, reaching up to 2% of the effective optical depth. These residuals likely result from uncertainties in the SO_2 cross sections' absolute values, wavelength assignments, and temperature dependencies, as well as possible contributions from uncertainties in the vertical distribution of SO_2 and volcanic ash, and from remaining uncertainties in GOME-2 radiometric and wavelength calibration.

4.2. Comparisons to Slant Column Density Retrievals

[49] Figure 3 shows monthly average retrieved SO_2 from the SCD/AMF and optimal estimation approaches for May 2008, using mostly clear sky ground pixels with cloud fractions (f_c) less than 0.2 and solar zenith angles (SZA) less than 70°. Several prominent SO_2 features are easily detected, including: pollution over eastern China, Mexico City, and the Highveld region in South Africa; volcanic emissions over Hawaii; and noise from the South Atlantic Anomaly over South America. Although both retrievals show slight background offsets, an uncorrected land-sea negative offset is more pronounced in the SCD/AMF results. The mean percent difference between the two retrieval approaches is also plotted for individual measurements with SO_2 greater than 1 DU.

[50] The mean agreement for individual measurements is generally very good over the severely polluted area of eastern China, with individual OE retrievals usually agreeing with the SCD/AMF retrieval to within 10%. Even at higher cloud fractions (up to f_c = 0.5), correlations between the two algorithms remain strong for this polluted region

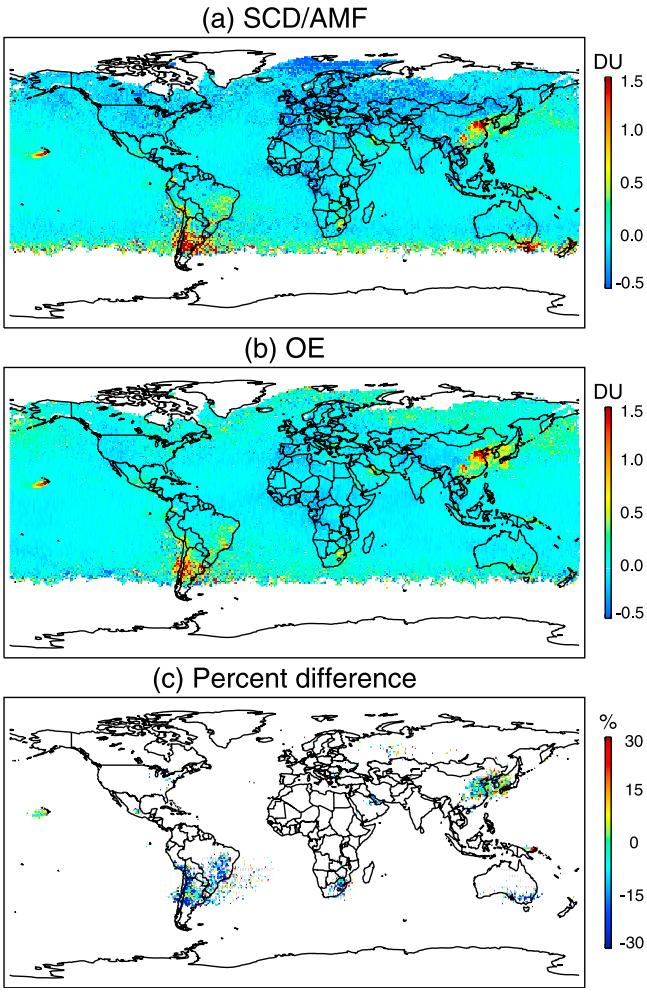

Figure 3. Monthly mean GOME-2 SO_2 vertical column density (VCD) for May 2008 on a 1° × 1° grid derived from (a) slant column density (SCD) retrieval, (b) optimal estimation retrieval, and (c) mean percent difference of Figure 3b minus Figure 3a for individual measurements with SO_2 VCD > 1 DU, at grid boxes with at least five such measurements. The mean is calculated using ground pixels with cloud fractions < 0.2 and solar zenith angles (SZA) < 70°.

and there is negligible bias between retrievals. (Bias between the two methods in this region remains low even up to f_c = 1; however, random uncertainties on individual measurements are significant at large cloud fractions, as are systematic uncertainties that may cause bias in both retrievals relative to the true SO_2 amount.) Certain geographic areas of anthropogenic pollution show larger biases between the two algorithms, with individual differences of up to ±40%, and with a more common tendency of the OE algorithm to underestimate relative to the SCD/AMF algorithm near sources, and overestimate in regions of transported SO_2. Volcanic effusive eruptive emissions from Hawaii agree quite well between the two retrievals (within 15%), although the OE retrieval is typically 10%–40% higher in the regions of very strong SO_2 columns (>5 DU) near the source. This relative enhancement of the OE retrieval is found in other regions where GEOS-Chem predicts SO_2 aloft, including the pollution outflow regions near China and South Africa. Generally, differences are within systematic uncertainties for the retrievals. Systematic differences are likely caused in part by several error sources discussed further in section 5, including the treatment of aerosols and the use of a predetermined surface albedo (SCD/AMF) versus a retrieved albedo (OE), as well as from the use of the FRESCO versus retrieved cloud fraction, SO_2 cross section temperature dependence, remaining background offset, and the consideration of a varying AMF across the wavelength fitting window.

[51] Individual measurements from single orbits are illustrated in Figure 4, which shows three sample retrieval cases for GOME-2 SO_2 retrievals for anthropogenic pollution (eastern China, Figure 4a), effusive emissions from a continuously active volcano (Hawaii, Figure 4b), and an explosive volcanic eruption (Mount Kasatochi, Alaska, Figure 4c). Sample profiles for several individual measurements from these cases are shown in Figure 5. On the whole, the SCD/AMF and OE results including background and enhanced SO_2 for these individual orbits are well correlated and agree within 10%.

[52] Figure 4c shows vertical columns calculated using the model profile for the SO_2 volcanic plume from Mount Kasatochi in Alaska on 9 August 2008. This plume lay over an area of the Pacific which is usually unpolluted, and where the model profile is characteristic of a clean marine profile. In reality, SO_2 from the Kasatochi eruption likely lies in layers centered near 7 km and 12 km, with some SO_2 as high as 15–17 km [*Kristiansen et al.*, 2010]. Figure 4l also shows results from our retrieval of VCD using the OE algorithm with a simultaneous SO_2 plume altitude retrieval. The total VCD is greatly reduced with the plume at higher altitudes. Retrieved plume altitudes from this eruption and their associated uncertainties are discussed further in section 5. Although the SCD/AMF algorithm is not able to account for variations in AMF across the fitting region, the fair agreement with the OE results indicates the 319.7 nm wavelength used for single-wavelength AMF calculations is likely well chosen for producing reasonable VCDs from this fitting window for cases with significant SO_2 absorption.

4.3. Channels 1 and 2 Combined Retrievals

[53] The majority of retrievals in this paper are assessed using only channel 2 wavelengths, in order to develop a consistent retrieval method appropriate for the entire mission lifetime. However, data collected after the band 1A/1B division change on 10 December 2008 allows a retrieval combining more wavelengths from channels 1 and 2, with no effect on ground pixel resolution. Multichannel retrievals using the optimal estimation approach are already applied to GOME and OMI profile retrievals [*Liu et al.*, 2005, 2010]. The careful radiometric calibrations developed for GOME-2 multichannel ozone profile retrievals (Cai et al., manuscript in preparation, 2011) and the use of a full radiative transfer model now allow for a combined band 1B/2B SO_2 retrieval from GOME-2.

[54] Retrievals using combined wavelengths 290–312 nm (band 1B) and 312–330 nm (band 2B) show improvements in retrieval performance. Figure 6 shows an orbit from 1 May 2009 processed using the combined retrieval and demonstrates the resulting reduction in retrieval noise for one sample cross-track position, as well as the improvement in offset (the

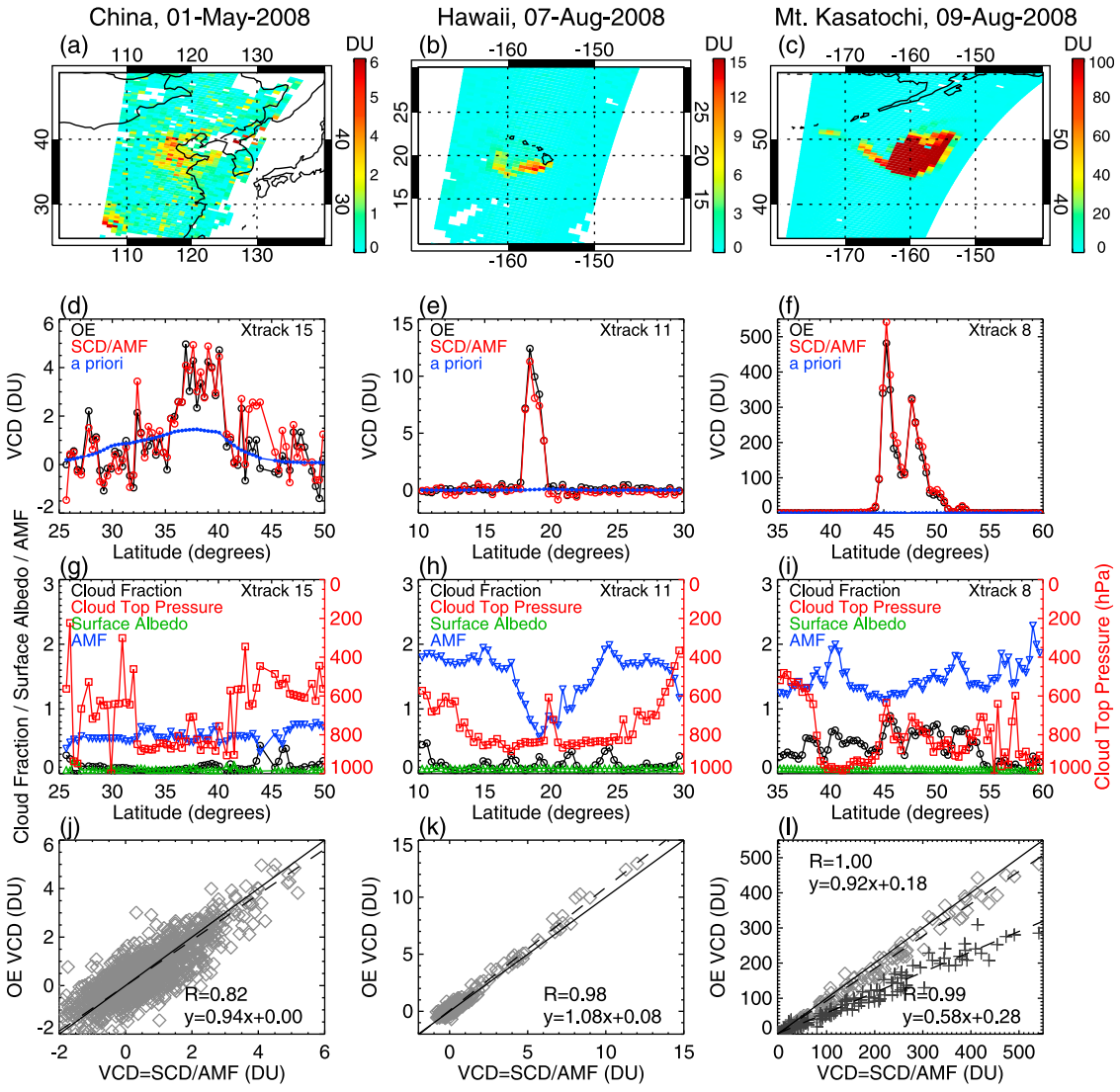

Figure 4. Sample SO_2 retrievals over a polluted region of China (1 May 2008, orbit 7947), effusive eruptive emissions over Hawaii (7 August 2008, orbit 9350), and an explosive volcanic eruption of Mount Kasatochi in Alaska (9 August 2008, orbit 9379) from the optimal estimation (OE) algorithm and a two-step slant column density and air mass factor (SCD/AMF) approach. Vertical column density of SO_2 from the OE algorithm for ground pixels with cloud fractions less than (a, b) 0.5 and (c) 1.0. (d–f) SO_2 VCD derived from the OE and SCD/AMF algorithms for one cross-track position as a function of latitude. (g–i) Cloud fraction, cloud top pressure, surface albedo, and AMF (at 319.7 nm) for those measurements. Scatterplot of VCDs derived using two approaches (diamonds) for all cross-track positions in the plotted latitude range for cloud fractions less than (j) 0.2, (k) 0.5, and (l) 1.0. Figure 4l also shows the OE VCDs derived simultaneously with plume altitude (crosses). Solid lines denote the 1:1 relationship. Dashed lines denote a reduced major axis linear regression.

band 2B retrieval was processed only after the application of a latitude-dependent offset of ~0.5 DU, while the band 1B/2B retrieval did not require an offset correction).

[55] Band 1B/2B retrievals generally have offsets at low solar zenith angles less than 0.05 DU. Precision on the retrievals is also improved, typically by 30%–40% at low solar zenith angles. Retrieved SO_2 values remain similar, with biases between the two retrievals generally within 15% for large SO_2 vertical columns (>1 DU), which is similar to biases observed by using different retrieval wavelength regions within channel 2 only (see Table 2). This improvement in precision may be particularly important for observations later in the mission because of GOME-2's total throughput degradation. Although not discussed in this paper, combined channel 1 and 2 retrievals should also improve retrievals of volcanic SO_2 at high altitudes, where weighting functions peak at shorter wavelengths than those at lower altitudes [see, e.g., *Yang et al.*, 2010].

5. Retrieval Characterization and Error Analysis

[56] The optimal estimation formulation provides a widely used method of formal characterization and error analysis

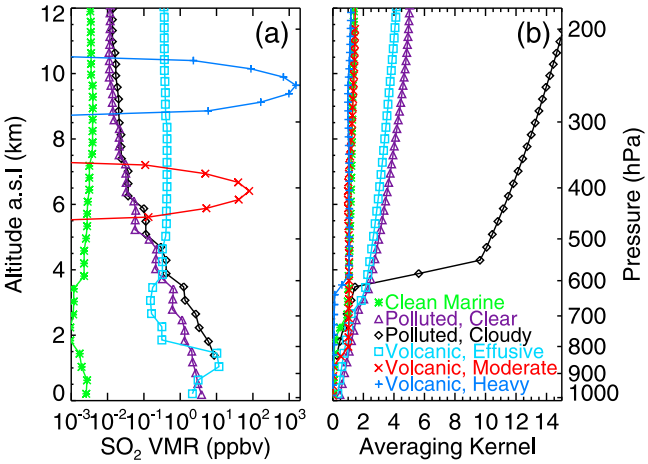

Figure 5. (a) SO_2 volume mixing ratio profiles and (b) averaging kernels for retrieval cases in Table 2 as a function of altitude above sea level (asl). Profiles and averaging kernels are plotted on a fine-altitude grid to show vertical structure.

[*Rodgers*, 2000]. Characterization and error estimates vary for individual measurements, and depend on model parameters including the SO_2 profile shape, cloud cover, cloud top pressure, albedo, solar zenith angle, viewing zenith angle, and contributions to the spectra from other absorbers and scatterers.

[57] In this section, we present characterization and error estimates for a selection of individual measurements from the orbits presented in Figure 4, as well as error assessments for global retrievals of SO_2, in addition to an assessment of altitude retrieval uncertainties and information content using the 9 August 2008 observation of SO_2 from the Mount Kasatochi eruption. Table 2 presents six retrieval cases for a detailed error analysis: a clean background case over the Pacific Ocean, anthropogenic pollution for clear ($f_c = 0.03$) and partly cloudy ($f_c = 0.42$) cases over China, a volcanic case for effusive eruptive emissions (Hawaii) where the anticipated profile is included in the GEOS-Chem model, and two observations of moderately and heavily polluted pixels from the Mount Kasatochi SO_2 plume.

5.1. Characterization

[58] The sensitivity of the solution state $\hat{\mathbf{x}}$ to the true state $\mathbf{x}$ is given by the averaging kernel $\mathbf{A}$, which is defined as

$$\mathbf{A} = \mathbf{G}_y \mathbf{K}_x = \frac{\partial \hat{\mathbf{x}}}{\partial \mathbf{x}}, \tag{3}$$

where $\mathbf{G}_y = \partial\hat{\mathbf{x}}/\partial\mathbf{y} = (\mathbf{K}_i^T \mathbf{S}_\epsilon^{-1} \mathbf{K}_i + \mathbf{S}_a^{-1})^{-1} \mathbf{K}_i^T \mathbf{S}_\epsilon^{-1}$ is the contribution function matrix representing the sensitivity of the solution state to a change in the measurement $\mathbf{y}$, and $\mathbf{K}_x = \partial\mathbf{y}/\partial\mathbf{x}$ is the weighting function matrix.

[59] The averaging kernel is most often used in vertical profile retrieval characterization to describe the sensitivity of a retrieved layer to a change in the true profile [e.g., *Liu et al.*, 2005, 2010], which is indicative of the vertical resolution of a retrieval. The diagonal elements of $\mathbf{A}$ also represent the degrees of freedom for signal (DFS), or independent pieces of information, of a measurement at each retrieved layer. The trace of the matrix represents the overall DFS for the profile.

[60] In the case of column retrievals, the retrieved vertical column density $\hat{x}_c$ is represented only by one value of the solution state vector $\hat{\mathbf{x}}$. In the most general form of the retrieval, the number of elements in the true state $\mathbf{x}$ does not necessarily have to equal the number of elements in the retrieved state $\hat{\mathbf{x}}$. Using the formulation of the averaging kernel from equation (3), and with the total vertical column density defined as $x_c = \sum_z x_{c,z}$, we calculate an averaging kernel for the total vertical column's sensitivity to the true partial vertical columns using

$$\mathbf{A}_c = \frac{\partial \hat{x}_c}{\partial \mathbf{x}_c} = \mathbf{G}_c \mathbf{K}_c = \frac{\partial \hat{x}_c}{\partial \mathbf{y}} \frac{\partial \mathbf{y}}{\partial \mathbf{x}_c}, \tag{4}$$

where $\mathbf{x}_c$ represents the vector of individual partial columns, $x_{c,z}$, in the forward model. For an optically thin absorber (optical depths $\ll 1$, or roughly $VCD_{SO2} < 10$ DU), the values of the averaging kernel vector could also be approximated as the ratio of the AMF at each layer z to the total AMF [*Eskes and Boersma*, 2003]; however, the generalized equation (4) can account for nonlinear absorption under strong SO_2 loading, as well as include the effects of

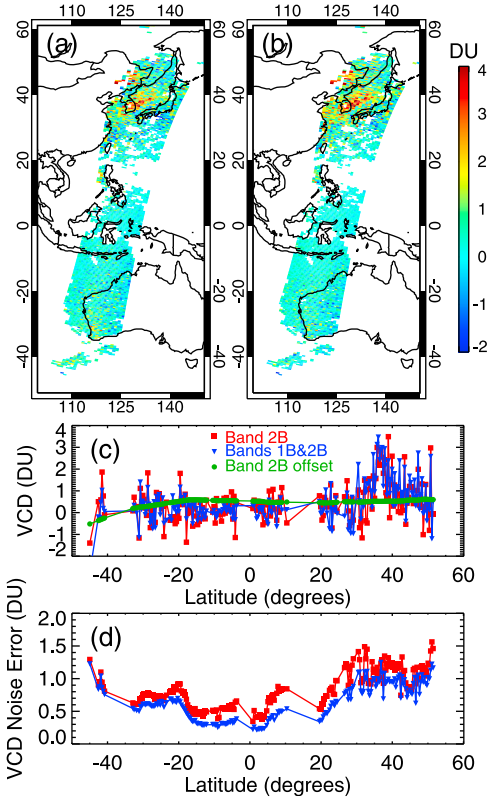

Figure 6. (a) Band 2B (312–330 nm) SO_2 retrievals for $f_c < 0.2$ on 1 May 2009, orbit 13132 (PPF 4.2.1), (b) as in Figure 6a but for combined band 1B (290–312 nm) and 2B (312–330 nm) retrieval, (c) retrieved SO_2 at cross-track position 16, as well as offset correction preapplied to band 2B retrieval, and (d) SO_2 retrieval noise uncertainty (see section 5.2.1). The band 2B retrieval was processed after the application of the latitude-dependent offset correction discussed in section 3.3. The combined band 1B/2B retrieval has not had an offset applied.

measurement noise and the wavelength dependence of the air mass factor.

[61] Figure 5 illustrates averaging kernels and profiles for the retrieval cases listed in Table 2. In the cases of marine background, anthropogenic pollution, and effusive volcanic emissions, the profiles are from the GEOS-Chem model, and scaled to the retrieved SO_2 vertical column density. In the two volcanic explosive eruption profiles, the profiles represent the Gaussian plume with FWHM = 0.5 km peaking at the retrieved plume altitude.

[62] The values of the averaging kernels represent the measurement's sensitivity to SO_2 at a particular altitude, and may be used to assess the uncertainty associated with a retrieved column value that may occur because of uncertainties in the shape of its true profile. For the clean marine background and the two plumes at higher altitude, averaging kernel elements above cloud tops are roughly 1–1.5 for all altitudes because the cloud reflectance makes retrievals much less altitude dependent. Below clouds, the value can be much less than one due to the shielding effects of clouds, depending on the cloud fraction. Where the pollution lies near the surface, there is a much greater dependence on altitude. For the cloud-free ($f_c = 0.03$) case of anthropogenic pollution, the mean element in the bottom 2.5 km is ~1, indicating an approximate 1:1 response for total SO_2 in the boundary layer. At higher altitudes, the averaging kernel elements grow rapidly, indicating possible significant enhancement of retrieved SO_2 in cases of up-lofted pollution or retrievals contaminated by transport of volcanic SO_2 if the model profile is assumed. The significant effect of clouds is demonstrated by the partly cloudy ($f_c = 0.42$) case of anthropogenic pollution, where a cloud layer at 642 hPa amplifies the averaging kernel elements above the cloud, and provides reduced sensitivity to individual layers below. Fortunately, in this case, most of the SO_2 likely lies entirely below the cloud; however, in cases of low-lying clouds, where some SO_2 could be at or above the cloud altitude, or in cases where SO_2 has been transported to higher altitudes, the retrieved VCD could be significantly enhanced relative to the true VCD.

5.2. Error Analysis

[63] *Rodgers* [2000] divides error contributions into four categories: (1) smoothing error, (2) model parameter error, (3) forward model error, and (4) retrieval noise. The smoothing error and retrieval noise may be determined directly from the retrieval, while the model parameter and forward model errors are determined separately.

5.2.1. Smoothing Error and Retrieval Noise

[64] The smoothing error and retrieval noise error contribute to the solution error

$$\hat{\mathbf{S}} = \left(\mathbf{K}^T \mathbf{S}_\epsilon^{-1} \mathbf{K}_i + \mathbf{S}_a^{-1}\right)^{-1}. \quad (5)$$

In our case, we estimate the retrieval noise error covariance $\mathbf{G}_y \mathbf{S}_\epsilon \mathbf{G}_y^T$ [*Rodgers*, 2000], and then determine the so-called "smoothing error" using the solution error as the root sum of the squares of the smoothing and retrieval noise errors. The smoothing error is generally used in profile retrievals to describe the loss of fine structure in the solution from the observing system's finite vertical resolution [*Rodgers*, 2000]. In the case of the unconstrained retrieved SO_2 VCD, the smoothing error results from the inability of the retrieval to differentiate SO_2 VCD from other parameters, and hence represents the cross correlation with other retrieved parameters such as ozone and albedo. In the case of altitude retrievals, where we do constrain the retrieval using an a priori uncertainty, the smoothing error in altitude is primarily from the contribution of the altitude a priori error to the solution error.

[65] Figure 7 shows the smoothing (Figure 7c) and noise (Figure 7d) errors for individual measurements in one typical month for $f_c < 0.2$. In our VCD retrievals where the SO_2 a priori uncertainty is very large, the solution errors on average tend to be dominated by the retrieval noise, or precision. (As with most error estimates, this can vary between individual measurements. For instance, Table 2 shows two polluted cases over China where the smoothing error is similar to the noise error.) Smoothing error often dominates when the spectral signature of SO_2 is strong and relative noise error is reduced, such as in the case of the largest volcanic Hawaiian SO_2 emissions in Figure 7. The mean noise estimates vary significantly with location and depend primarily on profile shape, as well as total radiance (solar zenith angle). The 1σ standard deviation of SO_2 retrievals over clean surfaces is also a measure of precision. During mid-2008, the retrieval precision as predicted by the optimal estimation algorithm at low solar zenith angles over the clean marine background for a single measurement is 0.2–0.3 DU, depending on viewing zenith angle. The precision calculated using the 1σ variation on a series of such measurements is ~0.26 DU. By SZA = 70°, the precision has increased to ~1 DU. The precision changes with instrument degradation, reaching ~0.5 DU by late 2009 for clean marine background.

[66] The precision over land is much worse because of the decreased sensitivity to the enhanced surface layers in the model profile. It is ~0.7–1.5 DU in mid-2008 for regions such as the United States and eastern China, where the SO_2 profiles are heavily weighted to the surface, whether or not the region is actually polluted. Tests using data over the relatively clean western United States using the variance of many clean land background SO_2 retrievals provide a 1σ variation of ~0.8 DU for a precision estimate, which compares well with the OE algorithm's predicted precision of ~0.7–0.8 DU in this region. The agreement between predicted and estimated precisions indicates signal-to-noise values detailed in section 3.4.3 are likely well estimated.

[67] Figure 8 shows the retrieval noise uncertainty for individual SO_2 measurements versus cloud fraction for regions with limits shown in Figure 7d. In polluted regions, the retrieval noise uncertainty increases with increasing cloud fraction, as true SO_2 signal measurable below the cloud decreases, and the retrieval algorithm is required to make greater assumptions about the amount of SO_2 in the vertical column on the basis of the SO_2 profile. For the polluted areas of China and the United States shown in Figure 8, uncertainty due to noise is ~1.2 DU for $f_c < 0.2$, increasing to ~2 DU by $f_c = 0.5$. Above $f_c = 0.5$, error increases significantly. Error over the clean Pacific actually decreases slightly with increasing cloud fraction until $f_c = 0.7$ because of larger signal to noise from brighter scenes with greater cloud cover.

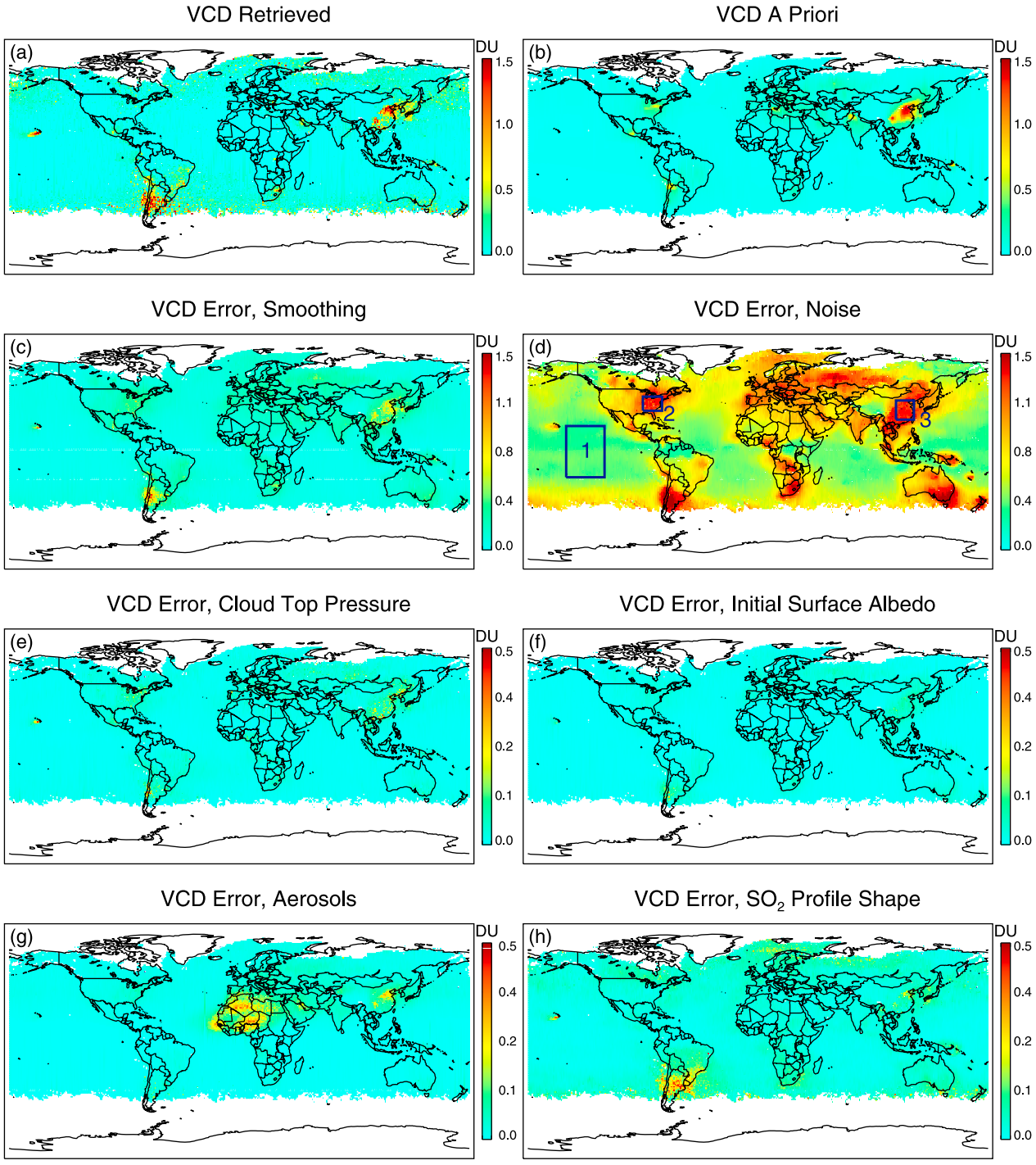

Figure 7. Monthly average SO_2 for May 2008 for $f_c < 0.2$ and SZA < 70° on a 1° × 1° grid showing (a) monthly average vertical column density, (b) a priori VCD from the GEOS-Chem model cubically interpolated from the 2° × 2.5° model grid, and uncertainties in individual measurements with cloud fractions less than 0.2 from errors of (c) smoothing, (d) retrieval noise, (e) cloud top pressure, (f) initial surface albedo, (g) aerosols, and (h) SO_2 profile shape. Figure 7d shows the limits of regions used to calculate uncertainties from noise as a function of cloud fraction in Figure 8 for the clean Pacific (box 1), the eastern United States (box 2), and eastern China (box 3).

5.2.2. Model Parameter Error

[68] Forward model parameter uncertainties and the resulting error contributions to specific measurement cases are listed in Table 2. We use an uncertainty of 53 hPa for cloud top pressure for the FRESCO cloud retrieval results [*Koelemeijer et al.*, 2001] and an uncertainty of 0.02 in the *Kleipool et al.* [2008] initial surface albedo. *Lee et al.* [2009] estimated the bias in AMFs from SO_2 profile uncertainty at

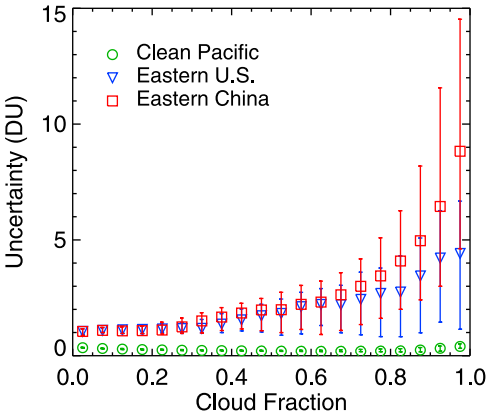

Figure 8. Monthly median uncertainty from noise on individual SO_2 measurements as a function of cloud fraction for regions with limits shown in Figure 7d. Error bars denote the 25th and 75th percentiles. All cloud altitudes are included in the calculation.

10% for clean background and anthropogenic pollution using comparisons between GEOS-Chem and aircraft in situ measurements. In order to estimate the local error introduced by the profile shape variability, we perform the retrieval for a set of individual daily profiles to compare with the retrieval using monthly mean profiles. The error estimates from the profile shape uncertainty are calculated using the combined errors of the bias (we assume a 10% bias in AMF corresponds to a 10% bias in our retrieved SO_2) and half the variability estimate [*Lee et al.*, 2009]. Uncertainties from aerosols are difficult to generalize because of a range of possible aerosol sizes and types; in this analysis we assess the effects of aerosols by turning GEOS-Chem aerosol fields off and on in the retrieval for the clean and anthropogenic pollution cases. We use 2005 aerosols in this analysis to avoid a large dust event over Asia in the May 2006 model results.

[69] Errors from aerosols in the volcanic cases are also difficult to assess as the aerosol distribution with altitude can be inhomogeneous, and aerosol type and size may vary. *Yang et al.* [2010] calculated uncertainties in retrieved VCD from ash and sulfate aerosols for an OMI measurement of a plume at 10 km to be less than 15% for most observing conditions with aerosol indices (AI) between −0.5 and 10, with plume height errors as large as 25% under the more extreme of those aerosol conditions. Errors increase substantially for large AIs (ash: >9, sulfate: <−0.7) when the aerosol layer is at or above the SO_2 plume. *Yang et al.* [2010] also assessed uncertainties from inhomogeneity of the observed scene, and found their OMI algorithm always underestimates SO_2 altitude for partially filled scenes. This scene inhomogeneity is most relevant at the edge of an SO_2 cloud.

[70] Uncertainties in *Bogumil et al.*'s [2003] SO_2 cross sections are estimated to be 4% (systematic) [*Vandaele et al.*, 2009] and 0.2% (random) for absolute values, and 0.01 nm (systematic) and 0.002 nm (random) for wavelength calibration. Uncertainties in ozone cross sections are estimated at 1% (systematic), 0.2% (random) for absolute values, and 0.002 nm (random). Errors introduced by uncertainties in the cross sections of NO_2 (5%), BrO (8%), and HCHO (10%) are negligible in the 312–330 nm wavelength fitting window.

[71] We also calculate model parameter uncertainties for systematic uncertainties in the temperature profile (3 K at each layer), the effect of modeling the volcanic plume using a FWHM of 2 km as opposed to 0.5 km, and for an uncertainty in the offset correction of 0.05 DU.

[72] Uncertainties in how the radiance spectrum is modeled are also considered under model parameter errors, including uncertainties in the radiance correction of 10% of the scaling used as the radiance calibration, a wavelength calibration uncertainty of 0.002 nm (random), and the slit function shape uncertainty, determined by calculating the spectrum using retrieved slit functions, and the slit function measured during the preflight calibration.

[73] We also include an estimate of uncertainties introduced in the fit from the choice of the retrieval wavelength window and the choice of polynomial order used for the radiance/irradiance calibration scaling. In all cases, this uncertainty is a significant contributor to the total uncertainty of the retrieval, in large part because of the decreased signal-to-noise ratio near 312 nm (where SNR ≈ 200), difficulties in instrument calibration near the end of band 2B (described in section 3.4) and the large dynamic range in radiance across the band because of ozone absorption and Rayleigh scattering.

[74] As evidenced in Table 2, the largest contributors to the model parameter error for the cloud-free (f_c = 0.03) polluted case are uncertainties in the initial surface albedo (which in its turn describes the initial cloud fraction), the SO_2 profile shape, the temperature profile, and the retrieval wavelength window and polynomial order choice. Aerosols are also a significant contributor for this particular ground pixel. For the partly cloudy case (f_c = 0.42), uncertainties introduced by the cloud top pressure and slit function are enhanced. When the plume is at a higher altitude, and/or considerable SO_2 signal is present, as with the volcanic plumes in Orbit 9379, the dependence on the cloud top pressure and slit shape is reduced. The geographic dependences of several of the most significant error sources are shown in Figures 7e–7h.

5.2.3. Forward Model Error

[75] Forward model error is the uncertainty introduced by using an approximation, **F**, of the true physics, **f**. In our retrievals, the only model error we can quantify is from any approximations for computational efficiency. The forward model errors introduced in the code are from approximations for the wavelength grid spacing of the forward model, number of vertical layers used in the modeled atmosphere, and the radiance polarization correction. Table 2 lists these forward model approximations and their resulting error contributions for several cases and shows the most significant forward model error is typically from the choice of the vertical grid used for radiative transfer calculations. The forward model approximations listed in Table 2 introduce uncertainties into the model, but unfortunately any increase in model resolution can significantly increase computation time. We choose these model approximations on the basis of a trade-off between model accuracy and computation time.

5.3. Sample Altitude Retrieval, Errors, and Information Content

[76] Figure 9 shows smoothing, measurement noise and total solution error for simultaneously retrieved values of

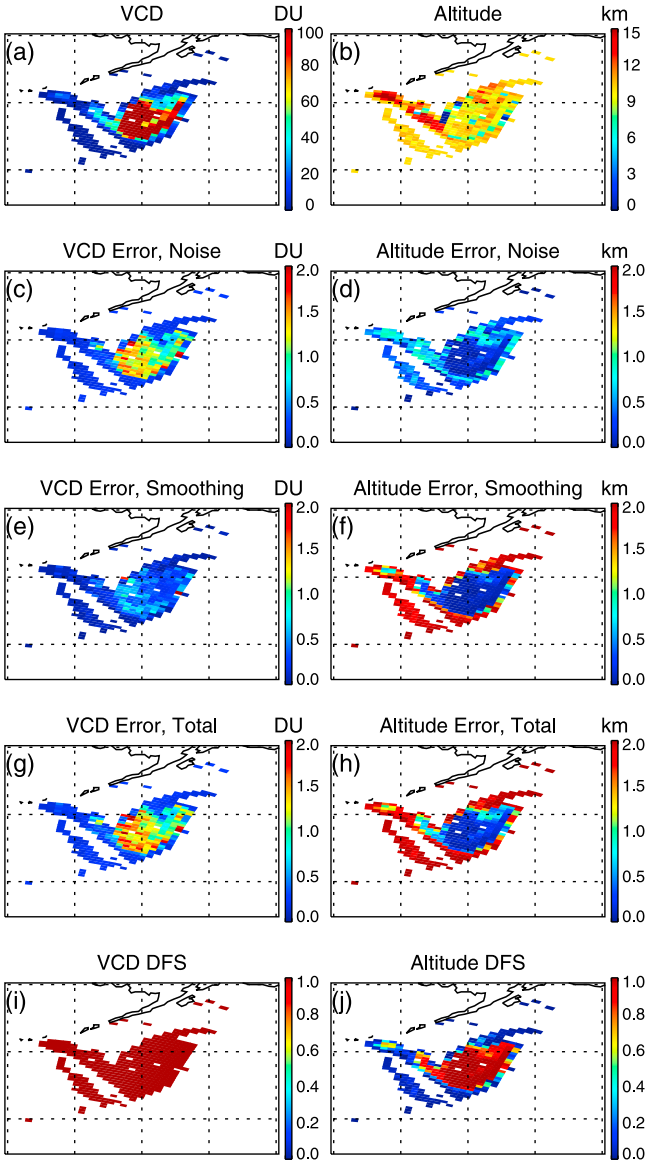

Figure 9. (a, b) SO_2 vertical column density and retrieved SO_2 plume altitude and their (c, d) measurement noise error, (e, f) smoothing error, (g, h) total solution error, and (i, j) the retrieval degrees of freedom for signal (DFS) for the Mount Kasatochi SO_2 plume on 9 August 2008 for SO_2 VCD greater than 1 DU, using z_{ap} = 10 km and $\epsilon_{z_{ap}}$ = 2 km.

SO_2 vertical column density and SO_2 plume altitude from the Mount Kasatochi volcanic plume on 9 August 2008.

[77] In all retrieved pixels, we have used an a priori of 10 km for the plume altitude with an a priori uncertainty of 2 km. Occasional pixel retrievals do not converge because of excessively large systematic residuals when SO_2 absorption is very large (most likely because of uncertainties in SO_2 cross sections; see section 4.1). Convergence on these retrievals may be achieved by relaxing the signal-to-noise estimates or convergence criteria, or decreasing the uncertainty on the a priori plume altitude. However, for consistency among retrievals, and for meaningful error and characterization assessments, we use the measurement's true signal-to-noise ratio and consistent a priori estimates. In the case of missing pixel values for the mass load calculation (see below), we interpolate the column value from neighboring pixels at the same cross-track position.

[78] The retrieved altitudes and their uncertainties are influenced by the relative combination of the a priori uncertainty and measurement signal-to-noise ratio. For the VCD solution, the noise dominates the solution error but remains small because of the large signal from SO_2. The uncertainty from noise in the altitude retrieval is also relatively small (typically 0.5–1 km), but the solution error approaches the a priori uncertainty (2 km) for measurements with small SO_2 absorption. For retrievals with very large amounts of SO_2 (>50 DU), the smoothing contribution to the altitude error approaches zero, indicating little influence from the a priori. Tests using a priori altitudes of 5 and 15 km indicate the retrieved altitudes of measurements with VCD > 50 DU are essentially uncorrelated to the a priori altitude value for this plume observation. Other sources of uncertainty in altitude retrievals, listed in Table 2, include aerosols, surface albedo, uncertainties in the vertical atmospheric model, including those from plume thickness and the temperature profile, instrument calibration, wavelength fitting window, and forward model error introduced by the choice of vertical grid spacing in the model. These uncertainty contributions are minimal in the case of very large SO_2 columns.

[79] The best indicator of the independence of a retrieval from its a priori is the degrees of freedom for signal (DFS) of a measurement, as plotted in Figures 9i and 9j, which demonstrate the number of independent pieces of information in the plume altitude retrieval. The DFS for the non-constrained VCD is always 1 and approaches 1 for the plume altitude retrieval for measurements with heavy SO_2 loading. Figure 10 shows the plume altitude DFS as a function of total SO_2 column. For these retrievals, the DFS is approximately 0.1 for measurements with VCD > 5 DU, indicating some information content for altitude information even at low SO_2 VCDs, and typically greater than 0.9 for measurements greater than 30 DU. Measurements with retrieved altitudes in the 6–8 km range at these VCDs typically have a DFS of 0.2 greater than those in the 15 km range, consistent with increasing altitude weighting func-

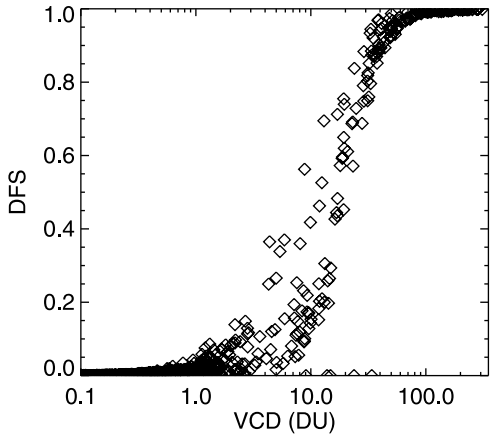

Figure 10. Retrieval degrees of freedom for signal (DFS) as a function of retrieved SO_2 VCD for the Mount Kasatochi SO_2 plume height on 9 August 2008, using z_{ap} = 10 km and $\epsilon_{z_{ap}}$ = 2 km.

tions for decreasing plume height [*Yang et al.*, 2009b]. The use of wavelengths less than 312 nm, available after 10 December 2008, should also increase information content, particularly in retrievals at higher altitudes [*Yang et al.*, 2009b]. Improvements in the accuracy of the SO_2 cross sections and/or instrument calibration may allow a larger altitude a priori error to be used in the retrieval, which would increase the DFS and allow improved retrievals of altitude with less dependence on the a priori value.

[80] The mass loading of SO_2 calculated from this retrieval is 1.6 Tg, in agreement with the SO_2 load from Kasatochi estimated at 1.6 Tg from both OMI [*Yang et al.*, 2010] and IASI [*Karagulian et al.*, 2010] on 9 August 2008, and a total load estimated at 1.2 to 1.7 Tg by other instruments and inverse transport modeling [see *Kristiansen et al.*, 2010, and references therein].

6. Comparisons With Surface Data

[81] In this section we compare GOME-2 SO_2 retrievals with surface observations of SO_2 over the continental United States and Canada. To our knowledge, the only peer-reviewed published validation of GOME-2 SO_2 measurements to date has been from measurements of the Mount Kasatochi plume by the CARIBIC aircraft over Europe compared to DOAS (Differential Optical Absorption Spectroscopy) GOME-2 retrievals [*Heue et al.*, 2010] for observations as large as 10 DU, which found well-correlated observations with a bias less than 10%. Here we use CASTNET, AQS, and NAPS surface data to examine GOME-2's potential for measuring anthropogenic SO_2.

[82] The EPA CASTNET data set represents weekly average background SO_2 at several sites throughout the United States. The EPA AQS and Environment Canada NAPS data sets typically include hourly data from a variety of locations, and include many urban measurements and measurements close to point sources of SO_2. *Lee et al.* [2010] compare AQS and NAPS data with OMI and SCIAMACHY retrievals for 2006. For this analysis, we also examine the rural and semirural sites of CASTNET, which may be better representative of the integrated SO_2 observed over GOME-2's large ground pixel size of 80×40 km^2.

[83] The GOME-2 surface SO_2 mixing ratio, S_{G2}, is determined from GOME-2 observations by scaling the retrieved total column, VCD_{G2}, by the ratio of the GEOS-Chem surface mixing ratio, S_{GC}, to the a priori GEOS-Chem total column, VCD_{GC}, using

$$S_{G2} = VCD_{G2} \frac{S_{GC}}{VCD_{GC}}. \quad (6)$$

The scaling factor for converting VCD measurements to surface mixing ratio in ppbv (parts per billion by volume) in the more polluted eastern United States is on the order of 10 ppbv/DU. For these retrievals, where individual measurement precision is on the order of ±1.2 DU (see Figure 7), we require approximately $N = 100$ samples to achieve a precision of ±1.2 ppbv in surface mixing ratio. We include GOME-2 data with center ground pixel locations within 40 km of each CASTNET, AQS, or NAPS site for 2008, which on average provide $N = 150$ observations per AQS site, and include only those sites with $N \geq 100$ coincidences. Data are excluded for certain days during July, August, and September 2008 where transported SO_2 is detectable from the Mount Okmok and Mount Kasatochi volcanic eruptions.

[84] Figure 11 shows annual mean modeled vertical column densities from GEOS-Chem for 2006 and the retrieved vertical column densities from GOME-2 for 2008 for measurements with $f_c < 0.2$ and SZA < 70°, as well as the surface mixing ratio in ppbv from GEOS-Chem, and the surface mixing ratio inferred from the GOME-2 column densities. GEOS-Chem values are given at GOME-2 measurement locations. Although the GOME-2 surface mixing ratios are directly inferred from the model, they are clearly correlated to the original retrieved vertical columns. Figure 11 also shows CASTNET and AQS and NAPS annual mean surface SO_2 for 2008 calculated at GOME-2 coincidences, and GOME-2 surface values calculated for observations within 40 km of each surface site.

[85] Figure 12 shows a scatterplot of GOME-2 SO_2 versus the in situ annual means at CASTNET, AQS and NAPS sites. GEOS-Chem surface SO_2 comparisons are also shown at these same GOME-2 locations. CASTNET annual means correlate well spatially with colocated GEOS-Chem 2006 annual means ($r = 0.78$, $N = 65$, $y = 2.73x + 0.35$) and GOME-2 SO_2 2008 annual means ($r = 0.85$, $N = 65$, $y = 2.49x + 0.19$), although both overestimate the CASTNET values. Comparisons with raw AQS and NAPS data, which often contain localized SO_2 sources, are indicative of GOME-2 subpixel and GEOS-Chem subgrid variabilities. Both GEOS-Chem ($r = 0.60$, $N = 438$, $y = 0.65x + 0.09$) and GOME-2 ($r = 0.40$, $N = 438$, $y = 0.58x + 0.27$) have difficulty fully reproducing the spatial variations of AQS and NAPS on a fine scale, but are able to predict the broad patterns of pollution over the eastern United States (Figure 11).

[86] The largest disagreements between GOME-2 and AQS and NAPS are where AQS or NAPS sites are located near large emission sources but background values tend to be low (such as in Billings, Montana, where five AQS sites are located within 10 km of a coal-burning power plant), and also several sites near the mid-Atlantic coastal regions from Virginia to Massachusetts, where GOME-2 follows the general pattern of high SO_2, but overestimates relative to the AQS measurements. The CASTNET coincident data clearly define the boundary at the edge of the AQS and NAPS data corresponding to the background relationship between the satellite observations and the surface in situ data.

[87] While there is significant scatter between GOME-2 values and AQS and NAPS data, the relative slope remains close to one (0.97) when large annual mean values (>10 ppbv, the maximum value of the GEOS-Chem annual mean in Figure 11c) of AQS and NAPS are excluded. GOME-2 is slightly better correlated ($r = 0.45$) with 24 h AQS and NAPS averages, but in this case clearly overestimates the in situ data by a factor of ~1.5. Averaging AQS data onto a $1° \times 1°$ grid improves the correlation to $r = 0.62$ ($N = 27$) when only grid boxes are compared containing at least three sites, with values averaged for sites that are located within 10 km of each other.

[88] Similar relationships have been previously observed with CASTNET, AQS, and NAPS comparisons with a different air quality model [*Moran et al.*, 2008]. In contrast, *Lee et al.* [2010] have shown highly correlated measurements

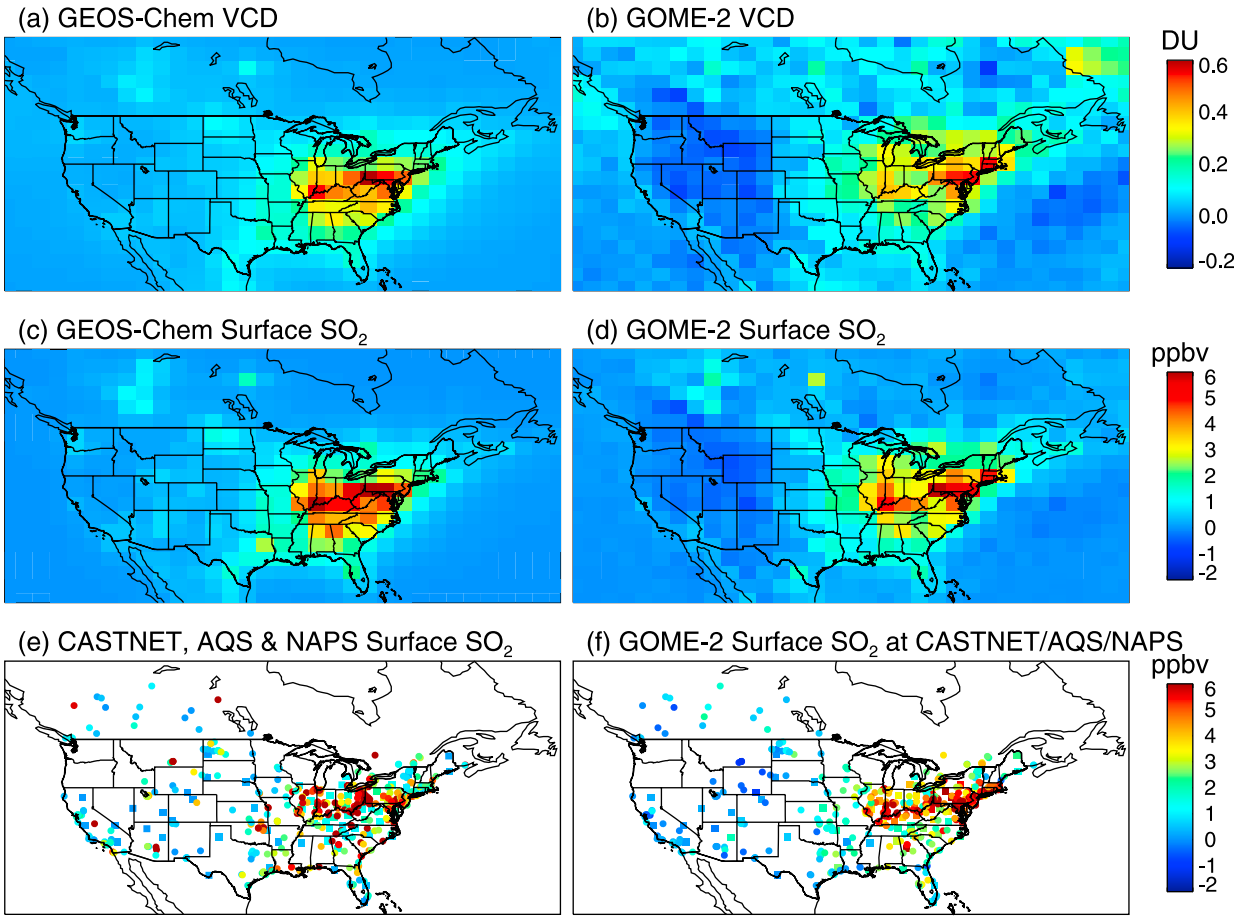

Figure 11. Total SO_2 vertical column density at GOME-2 measurement locations from (a) the GEOS-Chem model and (b) GOME-2 OE retrieval for $f_c < 0.2$, derived surface SO_2 at GOME-2 measurement locations from (c) GEOS-Chem and (d) GOME-2, (e) surface SO_2 from CASTNET (squares) and AQS and NAPS (circles) in situ observations, and (f) surface SO_2 from GOME-2 observations within 40 km of CASTNET, AQS, and NAPS sites. SO_2 from GEOS-Chem is the 2006 annual mean emissions estimate at GOME-2 measurement locations. GOME-2, CASTNET, AQS, and NAPS data are from 2008. CASTNET averages are calculated from weekly data, which overlap each GOME-2 overpass. AQS and NAPS averages are calculated from values within 1 h of GOME-2 overpass.

between SCIAMACHY and OMI and AQS and NAPS in situ measurements using a 15 km coincidence criterion, but include fewer AQS sites and only those measuring less than 6 ppbv at overpass times. As CASTNET data represents integrated SO_2 measured over a week, discrepancies may exist between CASTNET data and the modeled and satellite observations at local AM because of diurnal variability in boundary layer chemistry and mixing layer depth [*Lee et al.*, 2010]. It is also possible the actual profile shape may have lower relative SO_2 surface concentrations at these background sites than is predicted by the 2° × 2.5° GEOS-Chem grid.

[89] Measurements will also be affected by the large GOME-2 pixel size. Observations may include measurements of nearby localized SO_2 sources in background CASTNET-coincident GOME-2 ground pixels. Conversely, large emission sources may be minimized in averages of AQS and NAPS-coincident ground pixels because of the 40 km coincidence criterion. Additional error sources include transport and local meteorological conditions near overpasses, as well as the random and systematic uncertainties discussed in section 5.2, and a small remaining offset bias visible as a negative value over land.

7. Summary

[90] We have extended and optimized the SAO GOME and OMI ozone profile optimal estimation algorithm to retrieve SO_2 vertical columns from GOME-2. This approach implements the VLIDORT radiative transfer code and GEOS-Chem model profiles to implicitly include the effects of albedo, clouds, trace gas profiles, and wavelength dependencies in the retrieval. SO_2 retrieved using the optimal estimation formulation is similar to that from a two-step slant column and air mass factor calculation, with a tendency of the optimal estimation approach to produce slightly lower columns in regions close to anthropogenic sources (within ~10% in the case of eastern China), and higher for volcanic emissions and transported SO_2. Differences between SO_2 columns from the two algorithms are generally within estimated

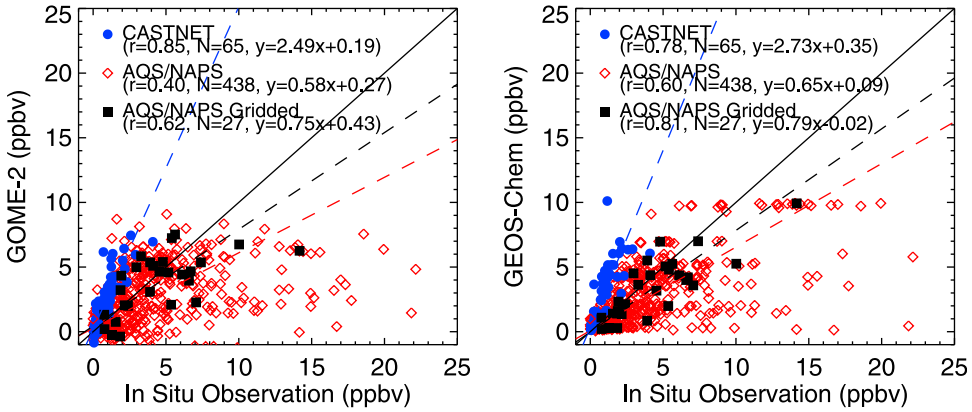

Figure 12. (left) Scatterplot of 2008 annual mean GOME-2 surface SO_2 versus CASTNET, AQS, and NAPS in situ data at GOME-2 coincidences and (right) GEOS-Chem 2006 mean at the same locations. The solid black line denotes the 1:1 relationship. Dashed lines denote reduced major axis linear regression. AQS and NAPS gridded data represent values averaged to a 1° × 1° grid, where each grid box contains at least three sites separated by at least 10 km.

uncertainties, and the slant column approach may be preferred for faster computation in certain cases and for continued operational retrievals. However, as a research algorithm, the optimal estimation approach allows easy extension to other wavelength windows and channels at even shorter wavelengths, a more accurate inclusion of the effects of ozone and an improved background offset in the retrieval, particularly at high latitudes, and the simultaneous retrieval of SO_2 plume altitude under certain conditions. The use of the optimal estimation retrieval for operational ozone profile measurements is currently under development, and it may be efficient to eventually integrate the SO_2 retrieval for a simultaneous SO_2 operational product.

[91] Error sources in clear sky retrievals in anthropogenic polluted regions are mainly from measurement noise, so-called "smoothing" error (correlations with other parameters), and uncertainties in surface albedo, profile shape, atmospheric temperature, wavelength fitting window, and aerosols. Uncertainty in cloud top pressure can dominate systematic uncertainties as cloud fractions increase. In this paper, we primarily use wavelengths 312–330 nm in channel 2, but retrieval precision can be improved by as much as 30%–40% by extending the retrieval to include band 1B wavelengths 290–312 nm after 10 December 2008.

[92] The algorithm is also extendable to include a direct retrieval of plume altitude under volcanic conditions where the plume altitude may be unknown. Unlike with simple vertical column retrievals, these retrievals require some constraint on SO_2 in the form of an assumed a priori plume altitude and a priori altitude uncertainty for retrieval stability. Uncertainties in the resulting retrieved vertical columns and plume altitude are dominated by the a priori uncertainty and uncertainties in aerosols, surface albedo, factors that determine the modeled plume structure (including the assumed plume thickness, temperature profile, and number of vertical layers used in the model calculation), and instrument calibration and wavelength fitting region. For our test case, using an a priori of 10 km and an uncertainty of 2 km, the degrees of freedom for signal for the altitude retrievals is greater than 0.1 for SO_2 columns greater than 5 DU and greater than 0.9 for SO_2 columns greater than 30 DU. Fitting residuals of up to 2% of the optical depth for large SO_2 loading during the Mount Kasatochi eruption in 2008 indicate improvements may be possible in SO_2 cross sections (in any or all of absolute values, wavelength calibration, and temperature dependence), and in GOME-2 calibration in this wavelength region.

[93] SO_2 surface mixing ratios are inferred from retrieved total vertical columns and GEOS-Chem model profiles and compared with surface in situ data from the EPA CASTNET and AQS and Environment Canada NAPS surface networks. GOME-2 is able to represent the spatial distribution of surface mixing ratios of background SO_2 determined from mostly rural CASTNET sites, although values are overestimated by a factor of approximately 2.5. On average, it is also able to represent the spatial distribution and absolute values of SO_2 from a variety of more polluted locations, although with much more variance than from the more remote background stations, but is generally is unable to differentiate SO_2 on small scales. More validation work and data, such as those from aircraft, would be useful to bridge the scales between satellite measurements and local in situ measurements for examining SO_2, which often has large but localized emission sources.

[94] This retrieval approach will be applied to retrieve SO_2 from other instruments observing the atmosphere in nadir backscatter, including OMI, GOME-1, SCIAMACHY, the Ozone Mapping and Profiler Suite (OMPS), and future geostationary instruments.

[95] **Acknowledgments.** The authors wish to thank the GOME-2 team at EUMETSAT for helpful discussions and data access, and the European Space Agency for their ongoing cooperation in the GOME program. CASTNET and AQS data are provided by the EPA. NAPS data are provided by the Analysis and Air Quality Division of Environment Canada. Research at the Smithsonian Astrophysical Observatory was funded by NASA and the Smithsonian Institution. This work was also partially supported by the NIMR/KMA project 'Development of meteorological resources for green growth'.

References

Afe, O. T., A. Richter, B. Sierk, F. Wittrock, and J. P. Burrows (2004), BrO emission from volcanoes: A survey using GOME and SCIAMACHY

measurements, *Geophys. Res. Lett.*, *31*, L24113, doi:10.1029/2004GL020994.

Bey, I., D. J. Jacob, R. M. Yantosca, J. A. Logan, B. D. Field, A. M. Fiore, Q. Li, H. Y. Liu, L. J. Mickley, and M. G. Schultz (2001), Global modeling of tropospheric chemistry with assimilated meteorology: Model description and evaluation, *J. Geophys. Res.*, *106*(D19), 23,073–23,095.

Bobrowski, N., C. Kern, U. Platt, C. Hörmann, and T. Wagner (2010), Novel SO_2 spectral evaluation scheme using the 360–390 nm wavelength range, *Atmos. Meas. Tech.*, *3*, 879–891.

Bogumil, K., et al. (2003), Measurements of molecular absorption spectra with the SCIAMACHY pre-flight model: Instrument characterization and reference data for atmospheric remote-sensing in the 230–2380 nm region, *J. Photochem. Photobiol. A*, *157*, 167–184.

Brion, J., A. Chakir, D. Daumont, J. Malicet, and C. Parisse (1993), High-resolution laboratory absorption cross section of O_3: Temperature effect, *Chem. Phys. Lett.*, *213*, 610–612.

Carn, S. A., L. L. Strow, S. de Souza-Machado, Y. Edmonds, and S. Hannon (2005), Quantifying tropospheric volcanic emissions with AIRS: The 2002 eruption of Mt. Etna (Italy), *Geophys. Res. Lett.*, *32*, L02301, doi:10.1029/2004GL021034.

Carn, S. A., A. J. Krueger, N. A. Krotkov, K. Yang, and P. F. Levelt (2007), Sulfur dioxide emissions from Peruvian copper smelters detected by the Ozone Monitoring Instrument, *Geophys. Res. Lett.*, *34*, L09801, doi:10.1029/2006GL029020.

Carn, S. A., A. J. Krueger, S. Arellano, N. A. Krotkov, and K. Yang (2008), Daily monitoring of Ecuadorian volcanic degassing from space, *J. Volcanol. Geotherm. Res.*, *176*, 141–150, doi:10.1016/j.jvolgeores.2008.01.029.

Chance, K., and R. L. Kurucz (2010), An improved high-resolution solar reference spectrum for Earth's atmosphere measurements in the ultraviolet, visible, and near infrared, *J. Quant. Spectrosc. Radiat. Transfer*, *111*, 1289–1295, doi:10.1016/j.jqsrt.2010.01.036.

Chance, K. V., and R. J. D. Spurr (1997), Ring effect studies: Rayleigh scattering, including molecular parameters for rotational Raman scattering, and the Fraunhofer spectrum, *Appl. Opt.*, *36*(21), 5224–5230.

Chance, K., P. I. Palmer, R. J. D. Spurr, R. V. Martin, T. P. Kurosu, and D. J. Jacob (2000), Satellite observations of formaldehyde over North America from GOME, *Geophys. Res. Lett.*, *27*(21), 3461–3464.

Chance, K., T. P. Kurosu, and C. E. Sioris (2005), Undersampling correction for array detector-based satellite spectrometers, *Appl. Opt.*, *44*(7), 1296–1304.

Clarisse, L., P. F. Coheur, A. J. Prata, D. Hurtmans, A. Razavi, T. Phulpin, J. Hadji-Lazaro, and C. Clerbaux (2008), Tracking and quantifying volcanic SO_2 with IASI, the September 2007 eruption at Jebel at Tair, *Atmos. Chem. Phys.*, *8*, 7723–7734.

Clarke, J. F., E. S. Edgerton, and B. E. Martin (1997), Dry deposition calculations for the clean air status and trends network, *Atmos. Environ.*, *31*(21), 3667–3678.

Clerbaux, C., P.-F. Coheur, L. Clarisse, J. Hadji-Lazaro, D. Hurtmans, S. Turquety, K. Bowman, H. Worden, and S. A. Carn (2008), Measurements of SO_2 profiles in volcanic plumes from the NASA Tropospheric Emission Spectrometer (TES), *Geophys. Res. Lett.*, *35*, L22807, doi:10.1029/2008GL035566.

Eisinger, M., and J. P. Burrows (1998), Tropospheric sulfur dioxide observed by the ERS-2 GOME instrument, *Geophys. Res. Lett.*, *25*(22), 4177–4180.

Eskes, H. J., and K. F. Boersma (2003), Averaging kernels for DOAS total-column satellite retrievals, *Atmos. Chem. Phys.*, *3*, 1285–1291.

European Organisation for the Exploitation of Meteorological Satellites (EUMETSAT) (2006), GOME-2 level 1 Product Generation Specification, *Rep. EPS.SYS.SPE.990011*, Darmstadt, Germany.

European Space Agency (1995), The GOME users manual, edited by F. Bednarz, *Eur. Space Agency Spec. Publ., ESA SP-1182*.

Faloona, I. (2009), Sulfur processing in the marine atmospheric boundary layer: A review and critical assessment of modeling uncertainties, *Atmos. Environ.*, *43*, 2841–2854, doi:10.1016/j.atmosenv.2009.02.043.

Forster, P., et al. (2007), Changes in atmospheric constituents and in radiative forcing, in *Climate Change 2007: The Physical Science Basis. Contribution of Working Group I to the Fourth Assessment Report of the Intergovernmental Panelon Climate Change*, edited by S. Solomon et al., pp. 129–234, Cambridge Univ. Press, Cambridge, U. K.

Haywood, J., and O. Boucher (2000), Estimates of the direct and indirect radiative forcing due to tropospheric aerosols: A review, *Rev. Geophys.*, *38*, 513–543.

Heue, K.-P., C. A. M. Brenninkmeijer, T. Wagner, K. Mies, B. Dix, U. Frieß, B. G. Martinsson, F. Slemr, and P. F. J. van Velthoven (2010), Observations of the 2008 Kasatochi volcanic SO_2 plume by CARIBIC aircraft DOAS and the GOME-2 satellite, *Atmos. Chem. Phys.*, *10*, 4699–4713.

Kalnay, E., et al. (1996), The NCEP/NCAR 40-year reanalysis project, *Bull. Am. Meteorol. Soc.*, *77*, 437–471.

Karagulian, F., L. Clarisse, C. Clerbaux, A. J. Prata, D. Hurtmans, and P. F. Coheur (2010), Detection of volcanic SO_2, ash, and H_2SO_4 using the Infrared Atmospheric Sounding Interferometer (IASI), *J. Geophys. Res.*, *115*, D00L02, doi:10.1029/2009JD012786.

Khokhar, M. F., C. Frankenberg, M. van Roozendael, S. Beirle, S. Kühl, A. Richter, U. Platt, and T. Wagner (2005), Satellite observations of atmospheric SO_2 from volcanic eruptions during the time-period of 1996–2002, *Adv. Space Res.*, *36*, 879–887.

Kleipool, Q. L., M. R. Dobber, J. F. de Haan, and P. F. Levelt (2008), Earth surface reflectance climatology from 3 years of OMI data, *J. Geophys. Res.*, *113*, D18308, doi:10.1029/2008JD010290.

Koelemeijer, R. B. A, P. Stammes, J. W. Hovenier, and J. F. de Haan (2001), A fast method for retrieval of cloud parameters using oxygen A band measurements from the Global Ozone Monitoring Experiment, *J. Geophys. Res.*, *106*(D4), 3475–3490.

Kristiansen, N. I., et al. (2010), Remote sensing and inverse transport modeling of the Kasatochi eruption sulfur dioxide cloud, *J. Geophys. Res.*, *115*, D00L16, doi:10.1029/2009JD013286.

Krotkov, N. A., S. A. Carn, A. J. Krueger, P. K. Bhartia, and K. Yang (2006), Band residual difference algorithm for retrieval of SO_2 from the Aura Ozone Monitoring Instrument (OMI), *IEEE Trans. Geosci. Remote Sens.*, *44*(5), 1259–1266, doi:10.1109/TGRS.2005.861932.

Krueger, A. J. (1983), Sighting of El Chichón sulfur dioxide clouds with the Nimbus 7 total ozone mapping spectrometer, *Science*, *220*, 1377–1379.

Lee, C., A. Richter, M. Weber, and J. P. Burrows (2008), SO_2 retrieval from SCIAMACHY using the weighting function DOAS (WFDOAS) technique: Comparison with standard DOAS retrieval, *Atmos. Chem. Phys.*, *8*, 6137–6145.

Lee, C., R. V. Martin, A. van Donkelaar, G. O'Byrne, N. Krotkov, A. Richter, L. G. Huey, and J. S. Holloway (2009), Retrieval of vertical columns of sulfur dioxide from SCIAMACHY and OMI: Air mass factor algorithm development, validation, and error analysis, *J. Geophys. Res.*, *114*, D22303, doi:10.1029/2009JD012123.

Lee, C., R. V. Martin, A. van Donkelaar, H. Lee, R. Dickerson, J. C. Hains, N. Krotkov, A. Richter, K. Vinnikov, and J. J. Schwab (2010), SO_2 emissions and lifetimes: Estimates from inverse modeling using in situ and global, space-based (SCIAMACHY and OMI) observations, *J. Geophys. Res.*, *116*, D06304, doi:10.1029/2010JD014758.

Liu, X., K. Chance, C. E. Sioris, R. J. D. Spurr, T. P. Kurosu, R. V. Martin, and M. J. Newchurch (2005), Ozone profile and tropospheric ozone retrievals from the Global Ozone Monitoring Experiment: Algorithm description and validation, *J. Geophys. Res.*, *110*, D20307, doi:10.1029/2005JD006240.

Liu, X., K. Chance, C. E. Sioris, and T. P. Kurosu (2007), Impact of using different ozone cross sections on ozone profile retrievals from Global Ozone Monitoring Experiment (GOME) ultraviolet measurements, *Atmos. Chem. Phys.*, *7*, 3571–3578.

Liu, X., P. K. Bhartia, K. Chance, R. J. D. Spurr, and T. P. Kurosu (2010), Ozone profile retrievals from the Ozone Monitoring Instrument, *Atmos. Chem. Phys.*, *10*, 2521–2537.

Martin, R. V., et al. (2002), An improved retrieval of tropospheric nitrogen dioxide from GOME, *J. Geophys. Res.*, *107*(D20), 4437, doi:10.1029/2001JD001027.

McLinden, C. A., S. C. Olsen, B. Hannegan, O. Wild, M. J. Prather, and J. Sundet (2000), Stratospheric ozone in 3-D models: A simple chemistry and the cross-tropopause flux, *J. Geophys. Res.*, *105*(D11), 14,653–14,665.

McPeters, R. D. (1993), The atmospheric SO_2 budget for Pinatubo derived from NOAA-11 SBUV/2 spectral data, *Geophys. Res. Lett.*, *20*(18), 1971–1974.

McPeters, R. D., G. J. Labow, and J. A. Logan (2007), Ozone climatological profiles for satellite retrieval algorithms, *J. Geophys. Res.*, *112*, D05308, doi:10.1029/2005JD006823.

Meller, R., and G. K. Moortgat (2000), Temperature dependence of the absorption cross sections of formaldehyde between 223 and 323 K in the wavelength range 225–375 nm, *J. Geophys. Res.*, *105*(D6), 7089–7101.

Moran, M. D., et al. (2008), Comprehensive surface-based performance evaluation of a size- and composition-resolved regional particulate-matter model for a one-year simulation, in *Air Pollution Modeling and Its Application XIX*, edited by C. Borrego and A. I. Miranda, pp. 434–442, Springer, Dordrecht, Netherlands.

Munro, R., M. Eisinger, C. Anderson, J. Callies, E. Corpaccioli, R. Lang, A. Lefebvre, Y. Livschitz, and A. Pérez Albiñana (2006), GOME-2 on MetOp, paper presented at the 2006 EUMETSAT Meteorological Satellite Conference, Eur. Org. for the Exploit. of Meteorol. Satell., Helsinki.

Notholt, J., et al. (2005), Influence of tropospheric SO_2 emissions on particle formation and the stratospheric humidity, *Geophys. Res. Lett.*, *32*, L07810, doi:10.1029/2004GL022159.

Palmer, P. I., D. J. Jacob, K. Chance, R. V. Martin, R. J. D. Spurr, T. P. Kurosu, I. Bey, R. Yantosca, A. Fiore, and Q. Li (2001), Air mass factor formulation for spectroscopic measurements from satellites: Application to formaldehyde retrievals from the Global Ozone Monitoring Experiment, *J. Geophys. Res.*, *106*(D13), 14,539–14,550.

Pope, C. A., III, and D. W. Dockery (2006), Health effects of fine particulate air pollution: Lines that connect, *J. Air Waste Manage. Assoc.*, *56*, 709–742.

Richter, A. (2009), Algorithm theoretical basis document for the GOME-2 rapid volcanic SO_2 product, report, Inst. of Environ. Phys., Univ. of Bremen, Bremen, Germany.

Rodgers, C. D. (2000), *Inverse Methods for Atmospheric Sounding: Theory and Practice*, World Sci., Singapore.

Siddans, R., B. J. Kerridge, B. G. Latter, J. Smeets, G. Otter, and S. Slijkhuis (2006), Analysis of GOME-2 slit function measurements, final report, contract EUM/CO/04/1298/RM, Eur. Org. for the Exploit. of Meteorol. Satell., Darmstadt Germany.

Sioris, C. E., and W. F. J. Evans (2000), Impact of rotational Raman scattering in the O_2 *A* band, *Geophys. Res. Lett.*, *27*(24), 4085–4088.

Spurr, R. J. D. (2006), VLIDORT: A linearized pseudo-spherical vector discrete ordinate radiative transfer code for forward model and retrieval studies in multilayer multiple scattering media, *J. Quant. Spectrosc. Radiat. Transfer*, *102*, 316–342, doi:10.1016/j.jqsrt.2006.05.005.

Thomas, W., T. Erbertseder, T. Ruppert, M. van Roozendael, J. Verdebout, D. Balis, C. Meleti, and C. Zerefos (2005), On the retrieval of volcanic sulfur dioxide emissions from GOME backscatter measurements, *J. Atmos. Chem.*, *50*, 295–320, doi:10.1007/s10874-005-5544-1.

Valks, P., D. Loyola, N. Hao, M. Rix, and S. Slijkhuis (2009), Algorithm theoretical basis document for GOME-2 total column products of ozone, NO_2, SO_2, BrO, H_2O, tropospheric NO_2 and cloud properties, *Rep. DLR/GOME-2/ATBD/01*, Deutsch. Zent. für Luft- und Raumfahrt, Oberpfaffenhofen, Germany.

Vandaele, A. C., C. Hermans, P. C. Simon, M. Carleer, R. Colin, S. Fally, M. F. Mérienne, A. Jenouvrier, and B. Coquart (1998), Measurements of the NO_2 absorption cross-section from 42000 cm^{-1} to 10000 cm^{-1} (238–1000 nm) at 220 K and 294 K, *J. Quant. Spectrosc. Radiat. Transfer*, *59*, 171–184.

Vandaele, A. C., C. Hermans, and S. Fally (2009), Fourier transform measurements of SO_2 absorption cross sections: II. Temperature dependence in the 29000–44000 cm^{-1} (227–345 nm) region, *J. Quant. Spectrosc. Radiat. Transfer*, *110*, 2115–2126, doi:10.1016/j.jqsrt.2009.05.006.

Wilmouth, D. M., T. F. Hanisco, N. M. Donahue, and J. G. Anderson (1999), Fourier transform ultraviolet spectroscopy of the $A\ ^2\Pi_{3/2} \leftarrow X\ ^2\Pi_{3/2}$ transition of BrO, *J. Phys. Chem. A*, *103*, 8935–8945.

World Meteorological Organization (2007), Scientific assessment of ozone depletion: 2006, *Global Ozone Res. Monit. Proj. Rep. 50*, Geneva, Switzerland.

Yang, K., N. A. Krotkov, A. J. Krueger, S. A. Carn, P. K. Bhartia, and P. F. Levelt (2007), Retrieval of large volcanic SO_2 columns from the Aura Ozone Monitoring Instrument: Comparison and limitations, *J. Geophys. Res.*, *112*, D24S43, doi:10.1029/2007JD008825.

Yang, K., N. A. Krotkov, A. J. Krueger, S. A. Carn, P. K. Bhartia, and P. F. Levelt (2009a), Improving retrieval of volcanic sulfur dioxide from backscattered UV satellite observations, *Geophys. Res. Lett.*, *36*, L03102, doi:10.1029/2008GL036036.

Yang, K., X. Liu, N. A. Krotkov, A. J. Krueger, and S. A. Carn (2009b), Estimating the altitude of volcanic sulfur dioxide plumes from space borne hyper-spectral UV measurements, *Geophys. Res. Lett.*, *36*, L10803, doi:10.1029/2009GL038025.

Yang, K., X. Liu, P. K. Bhartia, N. A. Krotkov, S. A. Carn, E. J. Hughes, A. J. Krueger, R. J. D. Spurr, and S. G. Trahan (2010), Direct retrieval of sulfur dioxide amount and altitude from spaceborne hyperspectral UV measurements: Theory and application, *J. Geophys. Res.*, *115*, D00L09, doi:10.1029/2010JD013982.

Z. Cai, Key Laboratory of Middle Atmosphere and Global Environment Observation, Institute of Atmospheric Physics, Chinese Academy of Sciences, Beijing 100029, China.

K. Chance, T. P. Kurosu, X. Liu, and C. R. Nowlan, Atomic and Molecular Physics Division, Harvard-Smithsonian Center for Astrophysics, 60 Garden St., MS-50, Cambridge, MA 02138, USA. (cnowlan@cfa.harvard.edu)

C. Lee, National Institute of Meteorological Research, Korea Meteorological Administration, 45 Gisangcheong-gil, Dongjak-gu, Seoul 156-720, South Korea.

R. V. Martin, Department of Physics and Atmospheric Science, Dalhousie University, 6300 Coburg Rd., Halifax, NS B3H 3J5, Canada.